

The *Spitzer*/IRAC view of black hole - bulge scaling relations

E. Sani,^{1,2*} A. Marconi,¹ L. K. Hunt,² G. Risaliti^{2,3}

¹*Dipartimento di Fisica e Astronomia, Università di Firenze, Largo E. Fermi 2, I-50125 Firenze, Italy*

²*INAF - Osservatorio Astrofisico di Arcetri, Largo E. Fermi 5, I-50125 Firenze, Italy*

³*Harvard-Smithsonian Center for Astrophysics, 60 Garden Street, Cambridge, MA 02138*

Released 2010 Xxxxx XX

ABSTRACT

We present a mid-infrared investigation of the scaling relations between supermassive black hole masses (M_{BH}) and the structural parameters of the host spheroids in local galaxies. This work is based on two-dimensional bulge-disk decompositions of *Spitzer*/IRAC 3.6 μm images of 57 galaxies with M_{BH} estimates. We first verify the accuracy of our decomposition by examining the fundamental plane (FP) of spheroids at 3.6 μm . Our estimates of effective radii (R_e) and average surface brightnesses, combined with velocity dispersions from the literature, define a FP relation consistent with previous determinations but doubling the observed range in R_e . None of our galaxies is an outlier of the FP, demonstrating the accuracy of our bulge-disk decomposition which also allows us to independently identify pseudobulges in our sample. We calibrate M/L at 3.6 μm by using the tight $M_{\text{dyn}}-L_{\text{bul}}$ relation (~ 0.1 dex intrinsic dispersion) and find that no color corrections are required to estimate the stellar mass. The 3.6 μm luminosity is thus the best tracer of stellar mass yet studied. We then explore the connection between M_{BH} and bulge structural parameters (luminosity, mass, effective radius). We find tight correlations of M_{BH} with both 3.6 μm bulge luminosity and dynamical mass ($M_{\text{BH}}/M_{\text{dyn}} \sim 1/1000$), with intrinsic dispersions of ~ 0.35 dex, similar to the $M_{\text{BH}}-\sigma$ relation. Our results are consistent with previous determinations at shorter wavelengths. By using our calibrated M/L, we rescale $M_{\text{BH}}-L_{\text{bul}}$ to obtain the $M_{\text{BH}}-M_\star$ relation, which can be used as the local reference for high- z studies which probe the cosmic evolution of M_{BH} -galaxy relations and where the stellar mass is inferred directly from luminosity measurements. The analysis of pseudobulges shows that 4 out of 9 lie on the scaling relations within the observed scatter, while those with small M_{BH} are significantly displaced. We explore the different origins for such behavior, while considering the possibility of nuclear morphological components not reproduced by our two-dimensional decomposition.

Key words: black hole physics -galaxies: bulges - galaxies:fundamental parameters - galaxies: nuclei - galaxies:photometry - infrared:galaxies

1 INTRODUCTION

Supermassive black holes (BHs) are believed to dwell in almost all galaxy spheroids (hereafter bulges) as a result of past quasar activity (Soltan 1982, Marconi et al. 2004, Shankar 2009 and references therein). A direct link between bulge formation and the growth of the central BHs has been inferred from tight relations between BH mass (M_{BH}) and the bulge structural parameters, such as velocity disper-

sion (σ , Ferrarese and Merrit 2000, Gebhardt et al. 2000), luminosity (L_{bul} , Kormendy & Richstone 1995, Marconi & Hunt 2003 - hereafter, MH03) and mass (Magorrian et al. 1998, MH03, Häring & Rix 2004, hereafter HR04).

The underlying physics is encoded not only in the slopes of the correlations, but also in the intrinsic or cosmic scatter (rms), i.e. the scatter not accounted for by measurement uncertainties. Particular care has been taken with its measurement and, for instance, over the last 15 years the intrinsic scatter of $M_{\text{BH}}-L_{\text{bul}}$ decreased from an initial value of $rms \sim 0.5$ dex (in $\log M_{\text{BH}}$, Kormendy & Richstone 1995) to $\sim 0.3 - 0.4$ dex (MH03, Gültekin et al. 2009, Hu 2009

* E-mail: sani@arcetri.astro.it

hereafter G09 and H09 respectively). $M_{\text{BH}}-\sigma$ is considered one of the tightest relations ($rms \sim 0.25-0.3$ dex, Tremaine et al. 2002, T02), suggesting that bulge dynamics or mass rather than luminosity are driving the correlations. Indeed the $M_{\text{BH}}-M_{\text{dyn}}$ relation has a scatter comparable with $M_{\text{BH}}-\sigma$ (~ 0.3 dex, MH03, HR04, H09 and references therein). Nonetheless, slopes and rms of scaling relations are still a subject of debate; an accurate assessment of the actual rms is indeed crucial to draw conclusions on the physical origin of the correlations and turns out to be fundamental to both constrain BH-galaxy evolutionary models and compute the space density of BHs (e.g. G09, Hopkins et al. 2007).

Since a successful theoretical model should be able to account for *all* empirical BH-bulge relations, discerning which are the truly fundamental ones, there has also been a growing interest in searching for all possible connections of the BH with other structural parameters. These include the effective radius R_e (MH03) and its various combinations with σ such as virial mass, gravitational binding energy of the host spheroid (e.g. MH03, Aller & Richstone 2007, H09, Feoli et al. 2010), thus leading to a possible fundamental plane for BHs (Barway & Kembhavi 2007, Hopkins et al. 2007).

To investigate the interplay between M_{BH} , bulge dynamics and luminosity, it is crucial (*i*) to perform a proper photometric decomposition of the galaxy components (e.g. disk, bulge, bar etc.) and (*ii*) to obtain good estimators of stellar mass (M_*), dynamical mass (M_{dyn}) and the galaxy mass-to-light ratio (M/L).

An accurate bulge-disk decomposition can be performed by simultaneously fitting multiple bi-dimensional components to galaxy images. To compute the bulge mass, one can apply the virial theorem which turns out to be quite accurate (Cappellari et al. 2006) but requires a spectroscopical estimate of the velocity dispersion in addition to the bulge effective radius R_e . Alternatively, one can estimate M_* by combining L_{bul} with a M/L ratio based on calibrated relations available in the literature (see, e.g., Bell & de Jong 2001, Bell et al. 2003, Cappellari et al. 2006). In this case, M_* can be affected by dust extinction, depending on wavebands, and by the assumption of a constant M/L over the entire galaxy. In any case, it is believed that M_* is more easily estimated than M_{dyn} especially at higher redshifts where it is the only host property not affected by strong biases (Merloni et al. 2010, Trakhtenbrot & Netzer 2010, Lamastra et al. 2010).

Recently, attention has been drawn to the coexistence of pseudobulges and BHs (Graham 2008b, Greene, Ho & Barth 2008, H09, Nowak et al. 2010, Erwin 2010). Pseudobulges are bulges which are photometrically and morphologically disk-like (possibly containing typical disk features such as bars, rings or ovals) and which present 'cool' kinematics, dominated by rotation (Kormendy & Kennicutt 2004). Apparently, pseudobulges follow their own relation with BHs, hosting less massive BHs than classical bulges (Greene, Ho, & Barth 2008, H09). Indeed, in these kind of structures, M_{BH} seems to better correlate with the small classical bulge component only (Nowak et al. 2010, Erwin 2010). However, these results are only based on a few pseudobulges (~ 5) which have been analyzed as a separate class, and the poor statistics preclude a firm conclusion.

In this paper we present a mid-infrared (MIR) view of

the M_{BH} -bulge scaling relations based on a 2D photometric decomposition of *Spitzer*/IRAC images at $3.6 \mu\text{m}$. The superb performance of *Spitzer*/IRAC (Fazio et al. 2004) provides images of unprecedented quality in the MIR for the 57 galaxies analyzed here, and IRAC sensitivity permits the clear identification of morphological features. Therefore we identify classical bulges and pseudobulges with our analysis and compare their properties with M_{BH} for one of the largest samples ever considered. $3.6 \mu\text{m}$ observations are an ideal tracer of M_* , and are less affected by extinction than shorter wavelengths.

Our aims are to:

- determine the bulge structural parameters with high accuracy;
- investigate the M_{BH} -bulge scaling relations and their intrinsic scatter, taking into account the nature of the bulge (classical vs pseudobulges);
- calibrate the M/L ratio thus supplying the reference $M_{\text{BH}}-M_*$ in the local Universe for studies of the M_{BH} -galaxy scaling relations at higher z , based on M_* derived from luminosity measurements (by, e.g., Merloni et al. 2010, Trakhtenbrot & Netzer 2010).

In Section 2 we describe sample selection, data reduction and the grid-method adopted to decompose the IRAC $3.6 \mu\text{m}$ images. We then present the fundamental plane (FP) for spheroids defined by the objects in our sample. M_{BH} -bulge scaling relations and the linear regression methods adopted to estimate slopes and intrinsic dispersion of the correlations are described in Section 3. Section 4 is dedicated to a discussion about (a) the utility of $M_{\text{BH}}-M_{\text{dyn}}$ as a benchmark to probe BH vs host galaxy co-evolution, and (b) pseudobulges location in the scaling relations.

Throughout this paper we assume the standard cosmology with $H_0 = 70 \text{ km s}^{-1} \text{ Mpc}^{-1}$, $\Omega_M = 0.3$, $\Omega_\Lambda = 0.7$.

2 DATA SELECTION AND ANALYSIS

In this section we describe the criteria adopted to select our sources (Section 2.1), the techniques adopted to co-add the basic calibrated data (BCD) provided by version 18.7 of the *Spitzer* pipeline (Section 2.2), and the 2D fitting procedure followed to decompose IRAC $3.6 \mu\text{m}$ images (Section 2.3). Finally Section 2.4 contains the analysis of the FP at $3.6 \mu\text{m}$.

2.1 Sample selection

We consider the samples compiled by G09 and H09 for a total of 64 galaxies. These authors have selected only galaxies with reliable M_{BH} estimates (i.e. by stellar or gas dynamics and masers). This is one of the largest samples used so far to investigate BH-galaxy scaling relations which also allows a consistent comparison of our results with previous works.

G09 and Batcheldor (2010) have recently shown that discarding sources whose sphere of influence is not spatially resolved can bias or even simulate the observed linear relations. Therefore, we do not apply any cut based on that criterion. To increase the number of objects with low M_{BH} , we add to the sample NGC3368 and NGC3489 whose M_{BH} is estimated in Nowak et al. (2010). These objects have also

OBSERVATIONS

Source Name (1)	PID (2)	Date (3)	Frame Time (4)	Frames (5)	Position (6)
Circinus	40936	2007-09-09	12	1	4
IC1459	20371	2005-11-28	2	1	22
IC2560	40936	2007-07-05	12	1	4
IC4296	20371	2006-02-13	2	1	22
NGC221	00069	2004-07-19	12	1	5
NGC524	50630	2008-09-18	30	1	5
NGC821	20371	2005-08-21	2	1	22
NGC1023	00069	2004-02-11	30	1	5
NGC1068	00032	2004-01-16	12	2	5
NGC1300	61065	2009-09-06	30	1	11
NGC1316	00159	2004-02-23	30	1	9
NGC2549	50630	2008-12-23	30	1	5
NGC2748	61063	2009-12-02	30	1	4
NGC2778	30318	2006-11-24	100	1	5
NGC2787	03674	2004-10-30	30	1	3
NGC2974	30318	2006-12-28	100	1	5
NGC3031	00159	2004-05-01	30	1	12
NGC3079	00059	2004-04-05	12	1	4
NGC3115	00069	2004-04-29	12	1	4
NGC3227	03269	2004-12-21	12	1	1
NGC3245	03674	2004-11-28	30	1	3
NGC3368	00069	2004-05-19	30	1	5
NGC3377	00069	2004-05-27	30	1	5
NGC3379	00069	2004-12-15	12	1	5
NGC3384	30318	2006-12-27	100	1	5
NGC3414	50630	2009-01-29	30	1	5
NGC3489	00069	2004-05-19	12	1	5
NGC3585	30318	2006-07-09	100	1	5
NGC3607	00069	2004-05-19	12	1	5
NGC3608	30218	2006-12-27	100	1	5
NGC3998	00069	2004-04-21	12	1	5
NGC4026	30318	2006-12-26	100	1	5
NGC4151	03269	2004-12-17	12	1	5
NGC4258	20801	2005-12-25	30	2	7
NGC4261	00069	2004-05-27	12	1	5
NGC4374	00069	2004-05-27	12	1	5
NGC4459	03649	2005-01-22	12	1	5
NGC4473	03649	2005-01-22	12	1	5
M87 ^a	03228	2005-06-11	30	1	5
	03228	2005-06-11	30	1	5
NGC4486A	03228	2005-06-11	30	1	5
NGC4552	00159	2004-05-27	30	1	7
NGC4564	20371	2006-02-09	2	1	22
NGC4594	00159	2004-06-10	30	1	6
NGC4596	03674	2005-06-10	30	1	3
NGC4621	03649	2005-06-10	12	1	5
NGC4649	00069	2004-06-10	12	1	5
NGC4697	03403	2005-06-17	30	1	5
NGC5077	00069	2005-05-11	12	1	5
CenA	00101	2004-02-11	12	1	5
NGC5576	03403	2005-07-15	30	1	5
NGC5813	00069	2004-02-17	12	1	5
NGC5845	20371	2005-08-23	2	1	22
NGC5846	00069	2004-03-09	12	1	5
NGC6251	02418	2004-12-16	30	2	6
NGC7052	30877	2006-11-26	30	1	5
NGC7457	30318	2006-07-12	100	1	5
NGC7582	03269	2004-11-27	12	1	1

Table 1. Observations Log. Columns: (1) Source name. ^a mean of 2 observations (see Section 2.2 for details). (2) Proposal identification number (PID). (3) Observing date. (4) Exposure time for each frame. (5) Numbers of frames. (6) Number of positions to realize the source maps.

a pseudobulge and their inclusion allows us to better investigate at $3.6 \mu\text{m}$ the discrepancies between pseudo and classical bulge properties found by H09 and Nowak et al. (2010).

We thus obtain a sample of 66 galaxies, 7 of which (CygnusA, NGC1399, NGC3393, NGC4291, NGC4342, NGC4742, NGC5252) have no $3.6 \mu\text{m}$ public *Spitzer*/IRAC observations. In addition, we exclude M31 because the available maps do not cover the entire galaxy and we exclude the Milky Way as there are no secure measurements of its $3.6 \mu\text{m}$ bulge properties. The final sample thus consists of 57 galaxies. Tables 1 and 2 provide the basic parameters of the observations together with distances, M_{BH} and σ measurements¹. To identify pseudobulges in $3.6 \mu\text{m}$ images we adopt a criterion based on the Sérsic index and examine *a posteriori* the sources location in the $3.6 \mu\text{m}$ FP of elliptical galaxies.

2.2 IRAC images

Given the wavelength dependence of the emission from stellar photospheres, the $3.6 \mu\text{m}$ IRAC band is the best suited for our study. In fact, the STARBURST99 models (Leitherer et al. 1999) show that only $\sim 10\%$ and even less of the emission in the $4.5 \mu\text{m}$ band is stellar, and that at longer wavelengths the fraction is even lower (Helou et al. 2004). Hence we used only channel 1 (centered at $3.55 \mu\text{m}$) basic calibrated data (BCD).

Individual BCD frames were processed with version 18.7 of the SSC pipeline. The image mosaicking and source extraction package (MOPEX, Makovoz & Marleau 2005) was used to co-add BCD frames for each source. Bad pixels, i.e. pixels masked in the Data Collection Event (DCE) status files and in the static masks (*pmasks*), were ignored. Additional inconsistent pixels were removed by means of the MOPEX outlier rejection algorithms. We relied on the dual outlier technique, together with the multi-frame algorithm. The frames were corrected for geometrical distortion and projected onto a North-East coordinate system with pixel sizes of 1.20 arcsec, equivalent to the original pixels. Mosaics for data images were realized with standard linear interpolation. The same was done for the uncertainty images, i.e. the maps for the standard deviations of the data frames. The signal-to-noise ratio in our post-pipeline MOPEX mosaics are comparable to or better than those in the SSC products. M87 has two maps with different spatial extension, thus we average them with a weighted mean where the weights are given by uncertainty images.

2.3 Image analysis

We use the public program GALFIT V.3 (Peng, et al. 2002, 2007) to perform a two-dimensional decomposition of $3.6 \mu\text{m}$ images in bulge/disk components. Besides the standard inputs (e.g. data, point spread function² (PSF) images etc.),

¹ We assume that the effective velocity dispersion σ_e is consistent, within the errors, with the central velocity dispersion σ_c and we refer to it as σ . This choice is supported by G09, whose Fig. 2 shows that no bias is implied by this choice.

² We use the instrumental PSF image provided by the SSC, after checking that its full width at half maximum (FWHM) is consistent with what observed for the foreground stars in our images.

GALFIT requires a standard-deviation image, used to give relative weights to the pixels during the fit, and a bad pixel mask. We therefore use the uncertainty data obtained from MOPEX as sigma images and construct a bad pixel frame masking out foreground stars, background galaxies and possible irregularly shaped regions such as dust lanes across the galaxy.

We choose the number and kind of model components on the basis of the Hubble morphological types (listed in Table 1) and after a visual inspection of the images. Thus, for elliptical galaxies we use a pure Sérsic profile, while for lenticular (S0) and spiral galaxies we add an exponential disk. In the case of barred galaxies (SB), we consider an additional Gaussian component, equivalent to a Sérsic profile with index $n = 0.5$. In some cases, even if the source is classified as a barred galaxy, the bar cannot be identified in the MIR (e.g. NGC2778). In these cases we do not add any Gaussian component to the model. In the case of active galaxies, we also include a nuclear point source to account for the emission of the active galactic nucleus (AGN).

The contribution of thermal dust to the observed emission at $3.6 \mu\text{m}$ can be powered by an active galactic nucleus (AGN) and/or star formation. The former can be accounted for by including a nuclear PSF in the model, while the latter can be masked out. Indeed intense star formation occurs in well-localized knots of emission, and does not affect the entire galaxy disk. Overall we estimate that hot dust can contribute no more than a few percent to the bulge (or disk) total luminosity and, given its localized nature, should not significantly affect the structural parameters derived from our global two-dimensional fits.

We fix the background in the fits, estimating it as the mean surface brightness (with the relative standard deviation) over an annular region surrounding the galaxy between 2-3 times the optical radius. Foreground sources such as stars or galaxies are not considered in the background calculation by means of a 2.5 sigma rejection criterion.

Some aspects of the photometric decomposition are potentially problematic. Due to the functional form of the Sérsic profile, the effective radius R_e is coupled to the Sérsic index n . To control this degeneracy we follow Hunt, Pierini & Giovanardi (2004, hereafter HPG04) and fit every galaxy with Sérsic indexes n fixed to values $n = 1, 1.5, 2, 2.5, 3, 3.5, 4, 5, 6, 7$, which reasonably span all galaxy morphologies. We then assume 0.5 as the error on the Sérsic index retrieved from the best fit (see below for the criteria defining the best model).

In addition, background measurements can be affected by galaxy extended emission; indeed, in several cases the faint tail of source emission covers most of the field-of-view (NGC3115, NGC4621, NGC4374, NCG5846, NGC7052 are some extreme examples). Thus for each galaxy, we fix three different background values: $s, s - \sigma_s$ and $s + \sigma_s$, where s and σ_s are the sky flux and its standard deviation estimated as described above. This allows to account for possible large variations of the background.

Once the number of components is defined, we run 30 different models; for each of the 10 fixed n values we use the 3 different background estimates. The free parameters are

SAMPLE PROPERTIES.

Source Name (1)	Type (2)	Distance (3)	M_{BH} (4)	σ (5)	$\log L_V$ (6)	$\log L_K$ (7)
Circinus	Sb	4.0	$0.017^{+0.004}_{-0.003}$	158 ± 18	-	10.03
IC1459	E4	30.9	$28^{+11}_{-12.0}$	340 ± 17	$10.96^{+0.06}_{-0.06}$	11.59
IC2560	SBb	40.7	$0.044^{+0.044}_{-0.022}$	144 ± 7	-	10.46
IC4296	E	50.8	13.5^{+2}_{-2}	226 ± 10	-	12.36
NGC221	E2	0.86	$0.031^{+0.006}_{-0.006}$	75 ± 3	$8.66^{+0.02}_{-0.02}$	8.83
NGC524	S0	33.6	$8.32^{+0.60}_{-0.37}$	235 ± 12	-	11.46
NGC821	E4	25.5	$0.42^{+0.28}_{-0.08}$	209 ± 10	$10.42^{+0.05}_{-0.06}$	10.8
NGC1023	SB0	12.1	$0.46^{+0.05}_{-0.05}$	205 ± 10	$10.17^{+0.10}_{-0.13}$	10.54
NGC1068	Sb	15.4	$0.086^{+0.003}_{-0.003}$	151 ± 7	$10.8^{+0.07}_{-0.09}$	10.82
NGC1300	SB(rs)bc	20.1	$0.71^{+0.09}_{-0.35}$	218 ± 10	-	-
NGC1316	SB0	19	$1.62^{+0.28}_{-0.27}$	226 ± 11	-	11.2
NGC2549	S0	12.3	$0.14^{+0.10}_{-0.12}$	145 ± 7	-	10.18
NGC2748	Sc	24.9	$0.47^{+0.38}_{-0.38}$	115 ± 5	-	-
NGC2778	E2	24.2	$0.16^{+0.90}_{-0.10}$	175 ± 8	$9.78^{+0.05}_{-0.06}$	-
NGC2787	SB0	7.9	$0.43^{+0.04}_{-0.05}$	189 ± 9	-	9.86
NGC2974	E4	21.5	$1.7^{+0.3}_{-0.3}$	227 ± 11	-	10.95
NGC3031	Sb	4.1	$0.80^{+0.2}_{-0.11}$	143 ± 7	-	10.44
NGC3079	SBcd	15.9	$0.025^{+0.002}_{-0.002}$	146 ± 7	-	10.26
NGC3115	S0	10.2	$9.6^{+5.4}_{-2.9}$	230 ± 11	$10.4^{+0.02}_{-0.02}$	10.46
NGC3227	SBa	17.0	$0.20^{+0.37}_{-0.08}$	133 ± 6	-	9.92
NGC3245	S0	22.1	$2.2^{+0.5}_{-0.5}$	205 ± 10	-	10.69
NGC3368	SABa	10.4	$0.075^{+0.015}_{-0.015}$	98.5 ± 5	-	-
NGC3377	E6	11.7	$1.1^{+1.1}_{-0.1}$	145 ± 7	$9.97^{+0.04}_{-0.04}$	10.22
NGC3379	E0	11.7	$1.2^{+0.8}_{-0.58}$	206 ± 10	$10.37^{+0.01}_{-0.01}$	10.96
NGC3384	SB0	11.7	$0.18^{+0.01}_{-0.03}$	143 ± 7	$9.90^{+0.08}_{-0.10}$	10.44
NGC3414	S0	25.2	$2.51^{+0.30}_{-0.31}$	205 ± 10	-	10.71
NGC3489	SB0	12.1	$0.06^{+0.012}_{-0.0012}$	91 ± 5	-	-
NGC3585	S0	21.2	$3.4^{+1.5}_{-0.8}$	213 ± 10	$10.65^{+0.07}_{-0.09}$	11.18
NGC3607	E1	19.9	$1.2^{+0.4}_{-0.41}$	229 ± 11	$10.58^{+0.04}_{-0.04}$	11.09
NGC3608	E1	23	$2.1^{+1.1}_{-0.7}$	182 ± 9	$10.35^{+0.04}_{-0.04}$	10.81
NGC3998	S0	14.9	$2.4^{+2.1}_{-1.8}$	305 ± 15	-	10.63
NGC4026	S0	15.6	$2.1^{+0.7}_{-0.4}$	180 ± 9	$9.86^{+0.07}_{-0.09}$	10.57
NGC4151	Sa	20.0	$0.65^{+0.07}_{-0.07}$	156 ± 8	-	10.27
NGC4258	SABbc	7.2	$0.378^{+0.001}_{-0.001}$	115 ± 10	-	9.93
NGC4261	E2	33.4	$5.5^{+1.1}_{-1.2}$	315 ± 15	$11.02^{+0.02}_{-0.02}$	11.42
NGC4374	E1	17	15^{+11}_{-6}	296 ± 14	$10.91^{+0.02}_{-0.02}$	-
NGC4459	E2	17	$0.74^{+0.14}_{-0.14}$	167 ± 8	$10.35^{+0.02}_{-0.02}$	10.58
NGC4473	E5	17	$1.3^{+0.5}_{-0.94}$	190 ± 9	$10.38^{+0.02}_{-0.02}$	10.92
M87	E1	17	36^{+10}_{-10}	375 ± 18	$11.1^{+0.02}_{-0.02}$	11.46
NGC4486A	E2	17	$0.13^{+0.05}_{-0.04}$	111 ± 5	$9.41^{+0.02}_{-0.02}$	10.19
NGC4552	E	15.3	$5.0^{+0.6}_{-0.4}$	252 ± 12	-	11.04
NGC4564	S0	17.0	$0.69^{+0.04}_{-0.10}$	162 ± 8	$9.77^{+0.11}_{-0.15}$	10.35
NGC4594	Sa	10.3	$5.7^{+4.3}_{-4.0}$	240 ± 12	$10.9^{+0.06}_{-0.06}$	-
NGC4596	SB0	18.0	$0.84^{+0.36}_{-0.25}$	136 ± 6	-	10.44
NGC4621	E5	18.3	$4.0^{+0.5}_{-0.4}$	225 ± 11	-	10.77
NGC4649	E2	16.5	21^{+5}_{-6}	385 ± 19	$10.99^{+0.02}_{-0.02}$	11.46
NGC4697	E6	12.4	$2.0^{+0.2}_{-0.2}$	177 ± 8	$10.44^{+0.04}_{-0.05}$	10.52
NGC5077	E3	44.9	$8.0^{+5.0}_{-3.3}$	222 ± 11	$10.74^{+0.05}_{-0.06}$	11.35
CenA	S0/E	4.4	$3.0^{+0.4}_{-0.2}$	150 ± 7	$10.66^{+0.03}_{-0.03}$	10.49
NGC5576	E3	27.1	$1.8^{+0.3}_{-0.4}$	183 ± 9	$10.43^{+0.05}_{-0.06}$	10.5
NGC5813	E1	32.2	$7.1^{+0.9}_{-0.6}$	230 ± 11	-	11.06
NGC5845	E3	28.7	$2.9^{+0.5}_{-1.7}$	234 ± 11	$9.84^{+0.05}_{-0.06}$	10.62
NGC5846	E0	24.9	$11.0^{+1.1}_{-1.0}$	237 ± 12	-	11.33
NGC6251	E1	106	$6.0^{+2.0}_{-2.0}$	290 ± 14	-	11.81
NGC7052	E3	70.9	$4.0^{+2.4}_{-1.3}$	266 ± 13	-	11.39
NGC7457	S0	14.0	$0.041^{+0.012}_{-0.017}$	67 ± 3	$9.42^{+0.04}_{-0.05}$	9.69
NGC7582	SBab	22.0	$0.55^{+0.26}_{-0.19}$	156 ± 19	-	-

Table 2. Columns: (1) galaxy name. (2) Hubble type taken from the Hyper-Leda catalogue. (3) Distance in Mpc. (4) M_{BH} in $10^8 M_{\odot}$, see G09, H09 and Nowak et al. (2010) for references on BH mass measurements. (5) Velocity dispersion in km/s. (6)-(7) logarithmic V- and K-band luminosities in solar units. The 1σ error of L_K is 10% (H09). All values in columns (4)-(7) are from G09 and H09 if not included in V-band sample, and are scaled from the original publications to our preferred distances (column 3) assuming the standard cosmology.

DECOMPOSITION PARAMETERS

Source Name (1)	n (2)	m_{bulge} (3)	R_e (4)	$(b/a)_b$ (5)	C_0 (6)	m_{disk} (7)	R_0 (8)	$(b/a)_d$ (9)	m_{bar} (10)	FWHM (11)	$(b/a)_{bar}$ (12)	m_{AGN} (13)
Circinus	2	5.48±0.04	0.21±0.01	0.68	0.2	4.4	1.58	0.39	-	-	-	-
IC1459	6	6.15±0.3	9.15±3.71	0.76	-0.14	-	-	-	-	-	-	12
IC2560	2	9.1 ± 0.7	5.43±2.84	0.37	0.62	9.0	6.18	0.57	-	-	-	10.8
IC4296	4	7.09±0.5	8.28±5.91	0.92	0.66	-	-	-	-	-	-	11.6
NGC221	4	5.2 ± 0.63	0.12±0.07	0.7	0.08	6.5	0.09	0.89	-	-	-	-
NGC524	3	7.01±0.19	4.37±2.54	0.95	-0.07	8.7	4.65	-	-	-	-	-
NGC821	7	6.9 ± 0.26	7.86±4.15	0.62	-0.19	-	-	-	-	-	-	-
NGC1023	3	6.7 ± 0.18	1.41±0.80	0.61	-0.55	6.67	48.51	0.3	9.01	1.13	0.55	-
NGC1068	1	6.15±0.05	0.73±0.02	0.73	0.19	6.1	1.76	0.81	-	-	-	7.37
NGC1300	3	8.40±0.33	8.32 ±1.30	0.29	0.0	7.56	7.21	0.74	-	-	-	-
NGC1316	5	4.7 ± 0.8	8.57±0.55	0.71	-0.15	6.91	11.52	0.63	-	-	-	11.13
NGC2549	7	8.32±0.13	0.69 ±0.15	0.5	-0.42	9	1.81	0.24	-	-	-	-
NGC2748	4	9.64±0.09	1.87 ±0.54	0.95	-0.31	8.72	1.9	0.24	-	-	-	-
NGC2778	2.5	10.44±0.15	0.29±0.05	0.73	0.09	9.74	1.22	0.79	-	-	-	-
NGC2787	3	7.57±0.57	0.60±0.19	0.62	0.0	8.07	1.12	0.52	11.5	0.17	0.11	12.3
NGC2974	3	7.28±0.14	2.83±0.61	0.67	-0.06	-	-	-	-	-	-	11.8
NGC3031	3	4 ± 0.31	2.53±0.87	0.62	-0.03	4.51	3.35	0.49	-	-	-	10.2
NGC3079	2	6.87±0.08	5.71±0.37	0.17	0.33	9.48	5.31	0.86	10	0.27	0.13	9.64
NGC3115	3	5.99±0.1	1.35±0.15	0.33	-0.62	6.69	3.4	0.41	-	-	-	-
NGC3227	4	7.27±0.5	6.83±2.27	0.49	0.18	9.44	2.36	0.44	-	-	-	-
NGC3245	2.5	8.73±0.2	0.49±0.04	0.58	-0.13	8.14	2.3	0.52	-	-	-	-
NGC3368	1	6.57±0.1	2.3 ±0.12	0.63	-0.13	6.83	6.17	0.58	7.25	0.7	0.55	-
NGC3377	6	6.93±0.18	3.13±0.88	0.55	0.03	-	-	-	-	-	-	-
NGC3379	5	5.85±0.16	2.61±0.64	0.88	0.03	-	-	-	-	-	-	-
NGC3384	2.5	8.11±0.07	0.25±0.01	0.76	-0.04	7.06	2.5	0.49	8.73	1.13	0.79	-
NGC3414	5	7.87±0.5	2.67 ±1.29	0.75	-0.44	9.28	3.04	0.87	12.4	0.29	0.36	-
NGC3489	1.5	8.3 ± 0.45	0.27±0.21	0.82	0.15	7.7	1.11	0.54	-	-	-	-
NGC3585	2.5	7.21±0.63	1.59±1.97	0.55	-0.28	7.08	5.25	0.61	-	-	-	-
NGC3607	5	6.44±0.25	4.3 ±2.02	0.83	0.0	-	-	-	-	-	-	12.9
NGC3608	6	7.19±0.23	6.29±2.51	0.79	0.12	-	-	-	-	-	-	-
NGC3998	1.5	8.14±0.05	0.34±0.36	0.82	0.07	7.75	1.51	0.79	-	-	-	10.3
NGC4026	3.5	8.08±0.18	0.86±0.30	0.60	0.0	8.36	2.34	0.16	-	-	-	-
NGC4151	3.5	8.13±0.41	0.52±0.42	0.87	0.07	8.17	2.99	0.61	-	-	-	14.6
NGC4258	2	5.27±0.08	3.9 ±0.42	0.46	0.18	8.73	6.84	0.66	-	-	-	9.6
NGC4261	4	7.23±0.15	3.66±2.80	0.80	0.0	8.81	6.65	0.99	-	-	-	13.09
NGC4374	7	5.06±0.04	8.73±1.00	0.90	0.0	-	-	-	-	-	-	11.7
NGC4459	2.5	7.7 ± 0.1	0.85±0.10	0.83	0.02	7.7	2.66	0.76	-	-	-	-
NGC4473	7	6.59±0.05	4.06±0.87	0.56	-0.07	-	-	-	-	-	-	-
M87	4	5.10±0.05	8.20±0.60	0.82	0.0	-	-	-	-	-	-	12.26
NGC4486A	2.5	9.04±0.08	0.59±0.07	0.8	0.03	-	-	-	-	-	-	-
NGC4552	4	6.65±0.08	1.8 ±0.81	0.92	-0.05	7.78	7.17	0.8	-	-	-	11.5
NGC4564	7	7.76±0.13	2.06±0.03	0.62	0.33	9.46	1.39	0.2	-	-	-	-
NGC4594	1.5	5.51±0.14	3.3 ±0.35	0.26	-0.93	5.79	2.74	0.61	6.32	7.79	0.71	9.64
NGC4596	3	7.6 ± 0.05	2.44±0.12	0.53	-0.23	7.66	4.91	0.83	11.76	0.05	0.99	-
NGC4621	5	6.22±0.1	5.46±1.09	0.63	-0.19	-	-	-	-	-	-	-
NGC4649	3	5.55±0.10	3.77±0.34	0.82	0.0	8.3	3.3	0.93	-	-	-	-
NGC4697	5	5.69±0.09	6.04±1.39	0.65	-0.1	-	-	-	-	-	-	-
NGC5077	6	7.61±0.26	6.35±2.34	0.71	0.11	-	-	-	-	-	-	15.53
CenA	3.5	3.49±0.27	2.21±1.2	0.83	0.0	4.16	3.92	5.20	0.50	-	-	10.2
NGC5576	7	7.26±0.15	4.51±1.29	0.71	0.03	-	-	-	-	-	-	-
NGC5813	6	6.52±0.18	17.4±3.80	0.78	0.1	-	-	-	-	-	-	-
NGC5845	3	8.96±0.02	0.51±0.02	0.67	-0.06	-	-	-	-	-	-	-
NGC5846	3	6.70±0.06	4.40±0.90	1	0.0	-	-	-	-	-	-	-
NGC6251	7	8.2 ± 0.19	21.8±7.71	0.84	-0.09	-	-	-	-	-	-	12.8
NGC7052	5	7.96±0.16	13.5±3.81	0.49	0.46	-	-	-	-	-	-	-
NGC7457	7	9.54±0.90	0.94±0.81	0.52	0.19	8.37	1.61	0.56	-	-	-	-
NGC7582	4	7.33±0.44	9.22±4.39	0.5	0.23	8.14	3.18	0.22	-	-	-	8.62

Table 3. Columns: (1) galaxy name. (2)-(6) bulge structural parameters: Sérsic index, 3.6 μm magnitude, effective radius in kpc, axis ratio, diskyness-boxiness ($C_0 < 0$ for diskly ellipsoids, $C_0 > 0$ for the boxy ones). (7)-(9) disk properties: 3.6 μm magnitude, scale length in kpc, axis ratio. (10-12) bar properties: 3.6 μm magnitude, FWHM in kpc, axis ratio. (13) AGN 3.6 μm magnitude.

the bulge and disk brightness³, their scale lengths, ellipticities, position angles and the bulge diskyness/boxyness. Additional free parameters can be the bar brightness, FWHM, ellipticity and position angle and/or the AGN point-source 3.6 μm magnitude. As starting guesses we use the axis ratio, the major axis position angle, provided by the HyperLeda⁴ database. The initial disk and bulge scale lengths (R_0 and R_e respectively), are proportional to the optical radius (R_{opt} listed in HyperLeda): $R_0 \sim 0.25R_{\text{opt}}$; the effective radius follows the bulge shape according to the Sérsic index $R_e \sim \frac{n}{10}R_{\text{opt}}$ for $n < 4$ and $R_e \sim 0.4R_{\text{opt}}$ for $n \geq 4$ (Giovanardi & Hunt 1988, Moriondo, Giovanardi & Hunt 1998).

As shown by HPG04, the bulge component influences the χ^2 value only in the inner region of the galaxy; indeed, the reduced χ^2 depends on n only at small distances (radii) from the center, while the large area of the disk strongly dilutes the influence of the bulge on the global χ^2 . Appendix A (available online) shows examples of the trend reduced χ^2 with radii for our galaxies outlining that fits with acceptable χ^2 values can differ significantly in the inner region where the bulge is important. Therefore, following HPG04, we selected the fits with the best n and sky values considering the lowest reduced χ^2 within half optical radius $R_{\text{opt},0.5}$. The fits are then considered reliable on the basis of circumnuclear flux conservation; the ratio between the inner counts in the residual and source images must lower than 0.05. This means that less than 5% of the central flux can be lost or introduced by the model. As described in the following section, the recovery of a tight FP at 3.6 μm shows the accuracy of our analysis in estimating bulge structural parameters.

The absolute errors on the free parameters are derived as the variations between the best fit values and the ones obtained from the model having the closest s , $s + \sigma_s$ or $s - \sigma_s$ value and the lowest possible reduced χ^2 within $R_{\text{opt},0.5}$ according to the criterion described above. With this choice we overestimate the statistical fit errors, but carefully constrain the effects due to an uncertain estimate of the background. The fit parameters and their uncertainties are listed in Table 3. See also Appendix A (available online) for further details on the error estimates.

2.4 The fundamental plane at 3.6 μm and the identification of pseudobulges

Early type galaxies and the bulges of disk galaxies follow the well known relations connecting their effective radius R_e , mean surface brightness $\langle I_e \rangle$ within R_e , and velocity dispersion σ (e.g. Djorgovsky & Davis 1987, Prugniel & Simien 1996, Jorgensen, Franx & Kjaergaard 1996, Burstein et al. 1997, Cappellari et al.2006). In particular, Jun & Im (2008, hereafter JI08) studied the FP at 3.6 μm considering a sample of elliptical galaxies spanning an order of magnitude in effective radii. Here, to analyze the bulge properties and verify the reliability of our analysis, we adopt the relation found by JI08:

$$\log R_e = 1.55 \times \log \sigma - 0.89 \times \log \langle I_e \rangle - 9.89, \quad (1)$$

where σ in km/s, R_e is in kpc and $\langle I_e \rangle$ in mag arcsec⁻².

Figure 1 shows the 3.6 μm FP for all our decomposed bulges obtained by using equation (1) (dashed black line). From Fig. 1 we can draw two main conclusions: (i) our bulges follow the 3.6 μm FP of elliptical galaxies with low dispersion, and (ii) pseudobulges (open red squares) lie on the FP within the observed dispersion. Indeed, (i) if we follow JI08 and apply a maximum likelihood method with a bootstrap resampling to account for errors, the intrinsic dispersion is: 0.20 ± 0.04 dex for the entire sample, and 0.11 ± 0.04 dex for non-active galaxies. The last result is consistent within the errors with JI08 ($rms = 0.09 \pm 0.04$, private communication). Thus the presence of an AGN can slightly worsen the 2D decomposition, introducing some degeneracy with the bulge component. Nevertheless, the low dispersion of the 3.6 μm FP for our bulges and the absence of strong outliers suggests that our 2D decomposition is reliable. A tight FP and its extension to reliably compact bulges then permit us to calibrate M/L (Fig. 4 and see Section 3.2).

A detailed analysis of the FP is beyond the scope of this paper. However, it should be noted that our sample spans an order of magnitude larger range in galaxy sizes, extending the FP to smaller galaxy radii than in JI08. This could be the origin of the possible small disagreement between the FP defined by our sources and the determination by JI08 (see Fig. 1).

Classical bulges and pseudobulges differ in morphology and dynamics: the first behave like early-type galaxies, scaled to small sizes, surrounded by a disk component. Classical bulges thus are either prolate or oblate spheroids and are kinematically⁵ hot, (tending to be pressure dominated with a stellar $V/\sigma < 1$). On the contrary pseudobulges are disk-like components with $V/\sigma > 1$ cold kinematics dominated by rotation and possibly containing disk features such as nuclear bars and rings as well as young stellar populations (Andredakis, Peletier & Balcells 1995, Fisher & Drory 2010, hereafter FD10, and references therein). A correlation between the bulge morphology and the Sérsic index has been proposed by considering the morphological properties of pseudobulges as shown in FD10. We thus follow the FD10 Sérsic index criterion to classify those bulges in spirals and lenticulars with $n < 2$ as pseudobulges. By means of the Sérsic index, we identify nine disk galaxies as hosting pseudobulges: Circinus, IC2560, NGC1068, NGC3079, NGC3368, NGC3489, NGC3998, NGC4258, NGC4594. The pseudobulges (ii) which we have identified are marked with open red squares in Fig. 1 and are not outliers of the 3.6 μm FP. This is not surprising since the physical meaning of the fundamental plane is that galaxies are virialized systems (Burstein et al. 1997) and this applies also to rotationally supported pseudobulges. Our sample partly overlaps the FD10 one, and for the 8 sources in common the classical versus pseudo classification of bulges is in perfect agreement.

³ To compute the magnitudes at 3.6 μm we adopt a zero point of 17.25 in Vega magnitudes, according to the IRAC photometric system (Reach et al. 2005).

⁴ <http://leda.univ-lyon1.fr/>

⁵ The bulge kinematics are defined according to Erwin (2010) where V is the stellar rotational velocity deprojected to its in-plane value and σ is the stellar velocity dispersion.

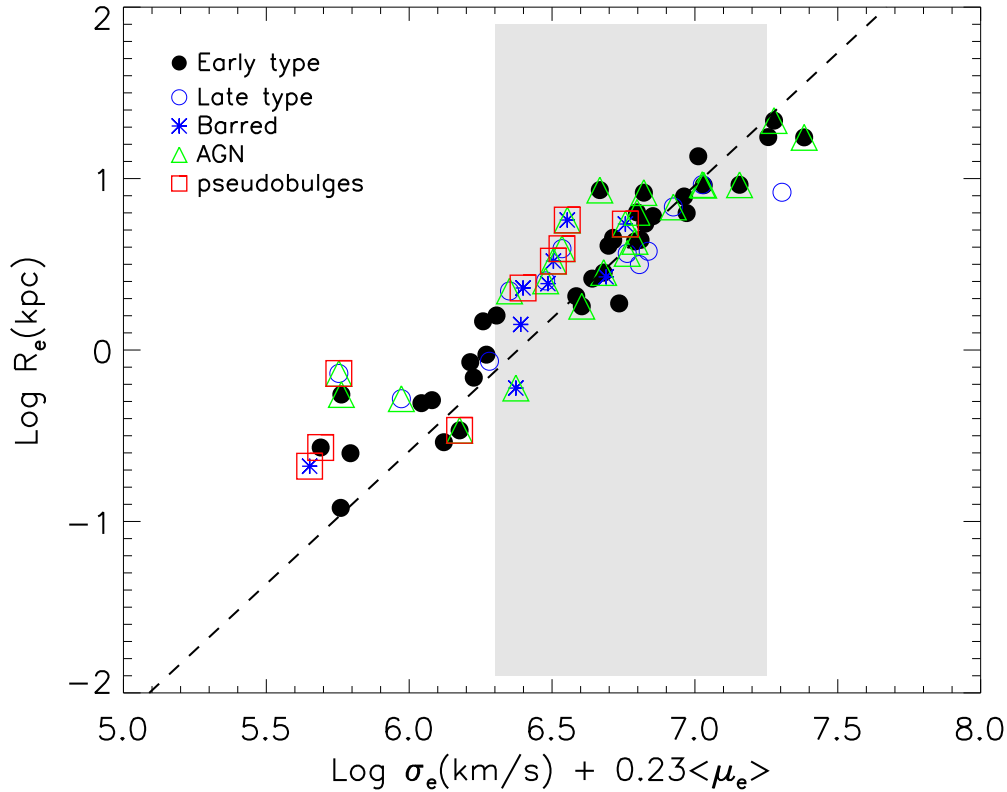


Figure 1. MIR fundamental plane for our decomposed bulges. The $3.6 \mu\text{m}$ FP coordinate axes are given by equation (1) (JI08), represented by the black dashed line. The bulge parameters are the effective radius R_e in kpc (Tab. 3), the velocity dispersion σ in km/s (Tab. 2) and the mean surface brightness within R_e , $\langle \mu_e \rangle = m_{\text{bulge}} + 2.5 \log[2\pi(b/a)_b R_e^2]$, where $(b/a)_b$ is the bulge axis ratio. $\langle \mu_e \rangle$ is expressed in $\text{mag}/\text{arcsec}^2$ (for a consistent comparison with JI08, Vega magnitudes in Tab.3 are converted to the AB photometric system as $m(\text{AB}) = m(\text{Vega}) + 2.79$). The color codes reflect the adopted fitting model, i.e. black points correspond to pure Sérsic profiles, blue symbols refer to Sérsic and an exponential disk (open circles), possibly with an additional Gaussian component (asterisks). The empty green triangles correspond to active galaxies, whose AGN emission is reproduced adding a point-like source to the models listed above. Open red squares highlight bulges with $n \leq 2$ which we thus classify as pseudobulges according to the FD10 criterion; no additional components are added to model these galaxies. The gray-shaded region highlights the range of velocity dispersion and surface brightness of the JI08 sample.

3 RESULTS

In the previous section we have verified the validity of our 2D decomposition by exploring the $3.6 \mu\text{m}$ FP for ellipticals, which turns out to be as tight as that observed by JI08 (private communication). Here we study the relations between M_{BH} and the bulge structural parameters listed in Tab. 2 and 3), respectively. To analyze the M_{BH} -bulge scaling relations, we adopt three different fitting methods:

1. a bisector linear regression (Akritas & Ber-shady 1996), which uses the bivariate correlated errors and intrinsic scatter (BCES) method. Whereas this method takes into account the intrinsic scatter, it does not allow any determination of it. Hence the intrinsic *rms* has been estimated with a maximum likelihood method assuming normally distributed values.

2. the linear regression FITEXY method as modified by T02, that accounts for the intrinsic scatter by adding, in quadrature, a constant value to the error of the dependent variable in order to obtain a reduced χ^2 of 1.

3. a Bayesian approach to linear regression, LINMIX_ERR (Kelly 2007), which accounts for measurement

errors, non-detections and intrinsic scatter to compute the posterior probability distribution of parameters.

The M_{BH} -bulge relations we fit are in the following form:

$$\log M_{\bullet}/M_{\odot} = \alpha + \beta \times (x - x_0), \quad (2)$$

where x is the logarithm of a measured bulge structural parameter expressed in solar units and x_0 is its mean value, used to reduce the covariance between the fit parameters. As described below, the three methods provide consistent results for the M_{BH} -bulge relations.

Since the LINMIX_ERR is argued to be among the most robust regression methods for reliable estimates of the intrinsic dispersion (Kelly 2007), we use it to obtain the final results on the M_{BH} -bulge scaling relations. We still use the BCES and FITEXY methods for comparison with previous works.

The fitting results are plotted in Fig. 2, 3, and 5, where we present the $M_{\text{BH}}-L_{\text{bul}}$, $M_{\text{BH}}-M_{\text{dyn}}$ and $M_{\text{BH}}-\sigma$ relations respectively. The $M_{\text{BH}}-\sigma$ relation is analyzed only to provide a consistent comparison with $M_{\text{BH}}-L_{\text{bul}}$ and $M_{\text{BH}}-M_{\text{dyn}}$ in terms of sample and fitting methods.

We exclude from the linear regressions the nine sources classified as pseudobulges. This allows us to verify, and possibly quantify, whether pseudobulges follow the same scaling relations as classical bulges. From a visual inspection of Fig. 2-5, pseudobulges with large BH masses ($M_{\text{BH}} > 10^7 M_{\odot}$) follow the relations while those with low BH masses deviate significantly from the scaling relations defined by classical bulges. Deviant pseudobulges are analyzed in the following sections and discussed in Section 4.

In the following, after describing in details the M_{BH} -bulge relations at 3.6 μm , we compare them with the published results obtained at shorter wavelengths. Finally in Section 3.4 we explore the possible M_{BH} correlation with σ and R_e separately as suggested by MH03, Hopkins et al. 2007, Graham 2008a.

3.1 M_{BH} versus 3.6 μm bulge luminosity

To construct the $M_{\text{BH}}-L_{3.6,\text{bul}}$ correlation, we compute the bulge 3.6 μm luminosity using the magnitudes obtained with the two-dimensional decomposition (see Section 2.3 for details) and reported in Tab. 3. To derive 3.6 μm luminosities in solar units we use the 3.6 μm Solar absolute magnitude obtained with a K-band value of 3.3 mag and a K-[3.6]=0.05 mag color correction (Allen 1976, see also Bessell & Brett 1988, Bell & De Jong 2001). The data for classical bulges are fitted with the three linear regression methods described at the beginning of this section. We obtain the following scaling relation of M_{BH} with 3.6 μm bulge luminosity (see Tab. 4 for the results from all fitting methods):

$$\begin{aligned} \log M_{\text{BH}}/M_{\odot} &= (8.19 \pm 0.06) + \\ &(0.93 \pm 0.10) \times [\log(L_{3.6,\text{bul}}/L_{3.6,\odot}) - 11] \\ &[rms = 0.38 \pm 0.05] \end{aligned} \tag{3}$$

All the fit parameters obtained with the three different methods are consistent within the errors (see Tab. 4, and Fig. 2). Our results are in excellent agreement with the $M_{\text{BH}}-L_{\text{bul},\lambda}$ obtained at shorter wavelengths. More specifically using the BCES and FITEXY results for the comparison, the intercept, slope and rms are fully consistent with the K-band measurements of MH03, Graham (2007), and H09. We find an intrinsic dispersion for the $M_{\text{BH}}-L_{3.6,\text{bul}}$ scaling relation with $rms = 0.35 \pm 0.05\text{dex}$ (BCES, FITEXY in Tab.4), consistent with the correlation in the K-band: $rms = 0.31$ and 0.36 dex in MH03 and H09 respectively. Optical observations in the V-band (Lauer et al. 2007, G09) produce slightly higher values for α and β . Different linear correlation coefficients can be due to a combination of factors: most obviously color corrections, but also incomplete sample overlap and the range of Hubble types (G09 fit only early types). Furthermore our $M_{\text{BH}}-L_{3.6,\text{bul}}$ is tighter than the V-band correlation whose rms is 0.38 ± 0.09 for early-type galaxies only. Moreover extinction can affect the luminosity, especially the V-band.

Figure 2 illustrates that 4 out of 9 pseudobulges (NGC3489, NGC3998, NGC4258, NGC4594) are consistent with the correlation for classical bulges, while the others (CIRCINUS, IC2560, NGC1068, NGC3079, NGC3368) are outliers, at more than 4σ below the LINMIX_ERR linear regression. The poor statistics for pseudobulges prevent us

from drawing firm conclusion on the physical nature of this behavior. Nevertheless we examine the possible disagreement also for the other M_{BH} linear regressions in Section 4.

3.2 M_{BH} versus bulge mass

In this section we first describe two methods to derive the bulge mass, and then relate M_{BH} with M_{dyn} and M_{\star} . Indeed one of our aims is to verify whether the 3.6 μm waveband is suitable to investigate the M_{BH} -bulge mass relations. We determine (i) the bulge dynamical mass M_{dyn} by applying the virial theorem (as in MH03, H09), and (ii) the bulge stellar mass by calibrating the M/L as a function of the 3.6 μm luminosity both with and without V-[3.6] and K-[3.6] colors. Thus (i) the bulge M_{dyn} is computed as follows:

$$M_{\text{dyn}} = \kappa R_e \sigma^2 / G, \tag{4}$$

where G is the gravitational constant, σ and R_e the velocity dispersion (in Tab.2) and the bulge effective radius (in Tab. 3) respectively. It is generally assumed that bulges behave as isothermal spheres and the factor κ is usually fixed at a value of 3 (Gebhardt et al. 2003) or 8/3 (MH03). However, since bulges are well reproduced by Sérsic profiles, κ is in general a function of the Sérsic index n . Cappellari et al. (2006), using full dynamical models, provide the $\kappa(n)$ relation for classical bulges and show that even the use of a constant average value of $\bar{\kappa} = 5$ can provide an accurate estimate of M_{dyn} to within 0.10 dex. We have therefore adopted $\bar{\kappa} = 5$.

The $M_{\text{BH}}-M_{\text{dyn}}$ bulge relation shown in Fig. 3A together with the three linear regressions. The M_{dyn} dependence for the 47 classical bulges is:

$$\begin{aligned} \log M_{\text{BH}}/M_{\odot} &= (8.20 \pm 0.06) + \\ &(0.79 \pm 0.09) \times [\log(M_{\text{dyn}}/M_{\odot}) - 11] \\ &[rms = 0.37 \pm 0.06] \end{aligned} \tag{5}$$

The three linear regressions are consistent within the errors (See Tab. 4, Fig. 3A). The $M_{\text{BH}}-M_{\text{dyn}}$ relation is rather tight with an $rms \sim 0.35$ dex from LINMIX_ERR, comparable to the scatter in the $M_{\text{BH}}-\sigma$ function (see Section 3.3). The $M_{\text{BH}}-M_{\text{dyn}}$ relations are in excellent agreement with the similar K-band analysis in MH03 and H09. The BCES regression is also consistent with a sample of 30 galaxies by HR04 although their slope is slightly superlinear.

The position of pseudobulges is the same observed in Fig. 2 and described in Section 3.1, where about half of the pseudobulges lie more than 4σ below the regression. The result for dynamical bulge mass can be compared with those for stellar mass to assess whether there are discrepancies between the two relations with M_{BH} .

To estimate (ii) the bulge stellar mass M_{\star} we have calibrated the M/L ratio at 3.6 μm through color corrections. It is known that the M/L ratio is wavelength dependent and not constant for a spiral galaxy in any waveband. M/L trends have been found to be minimized in the K-band (Bell & de Jong 2001, Bell et al. 2003). Published works assume a constant M/L with radius, while we are interested in the M/L for the bulge alone. The 3.6 μm wavelength is in principle a good tracer of stellar light for both young and old stellar populations as well, thus our data are expected to

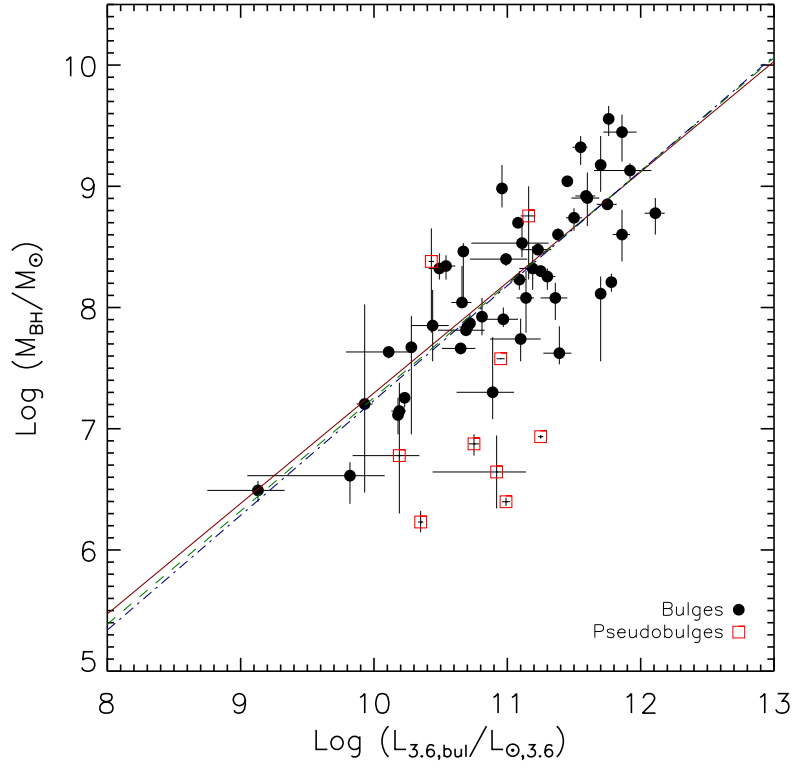


Figure 2. Scaling relations. The M_{BH} as a function of $3.6 \mu\text{m}$ luminosity. The linear regressions are shown as dot dashed blue, dashed green and red continuous lines respectively for the BCES, FITEXY and LINMIX_ERR methods and are obtained from classical bulges only (47 sources). Pseudobulges are open red squares.

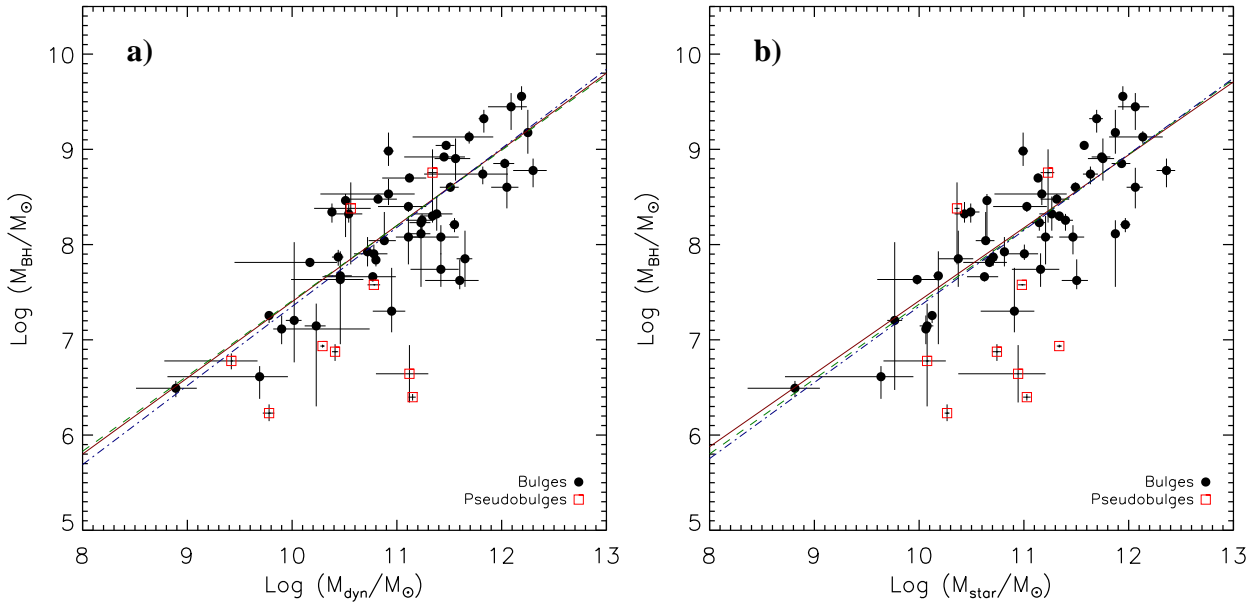


Figure 3. Scaling relations. The M_{BH} as a function of bulge dynamical mass (panel a) and bulge stellar mass (panel b). Pseudobulges are highlighted as red open squares. In panel (b) the M/L is from equation 6. See Section 3.2 and Fig. 4 for details on the M/L calibrations.

LINEAR REGRESSION COEFFICIENTS

$\log(M_{\text{BH}}) - \log(x)$	x_0	Method	α	β	rms	Ref.
$M_{\text{BH}}-L_{3.6,\text{bul}}$	11.0	BCES	8.18 ± 0.06	0.95 ± 0.10	0.35 ± 0.02	-
	11.0	FITEXY	8.21 ± 0.06	0.91 ± 0.10	0.35 ± 0.05	-
	11.0	LINMIX_ERR	8.19 ± 0.06	0.93 ± 0.10	0.38 ± 0.05	-
$L_{\text{bul},K}$	10.9	BCES	8.21 ± 0.07	1.13 ± 0.12	0.31	MH03 ^a
	10.9	FITEXY	8.29 ± 0.08	0.93 ± 0.10	0.33	G07
	10.9	BCES	8.38 ± 0.05	0.97 ± 0.08	0.36	H09
$L_{\text{bul},V}$	11.0	MAX. LIKE.†	8.95 ± 0.11	1.11 ± 0.18	0.38	G09 ^b
	10.3	BCES	8.41 ± 0.11	1.40 ± 0.17	-	L07‡
$M_{\text{BH}}-M_{\text{dyn}}$	11.0	BCES	8.18 ± 0.06	0.83 ± 0.08	0.33 ± 0.02	-
	11.0	FITEXY	8.20 ± 0.06	0.80 ± 0.08	0.35 ± 0.05	-
	11.0	LINMIX_ERR	8.20 ± 0.06	0.79 ± 0.09	0.37 ± 0.05	-
	10.9	BCES	8.28 ± 0.06	0.96 ± 0.07	0.25	MH03 ^a
	11.0	BCES	8.20 ± 0.10	1.12 ± 0.06	0.30	HR04
	10.9	BCES	8.61 ± 0.05	0.88 ± 0.06	0.27	H09
$M_{\text{BH}}-M_{\star}$	11.0	BCES	8.15 ± 0.05	0.80 ± 0.08	0.35 ± 0.03	-
	11.0	FITEXY	8.17 ± 0.06	0.77 ± 0.08	0.35 ± 0.05	-
	11.0	LINMIX_ERR	8.16 ± 0.06	0.79 ± 0.08	0.38 ± 0.05	-
	11.0	BCES	8.24 ± 0.05	1.07 ± 0.09	0.32	H09
$M_{\text{BH}}-\sigma$	200	BCES	8.27 ± 0.05	4.0 ± 0.3	0.32 ± 0.04	-
	200	FITEXY	8.30 ± 0.05	4.0 ± 0.3	0.30 ± 0.04	-
	200	LINMIX_ERR	8.29 ± 0.05	4.0 ± 0.4	0.33 ± 0.04	-
$M_{\text{BH}}-\sigma$	200	FITEXY	8.13 ± 0.06	4.0 ± 0.3	0.3	T02
$M_{\text{BH}}-\sigma$	200	MAX. LIKE.	8.23 ± 0.08	4.0 ± 0.4	0.31 ± 0.06	G09 ^b

Table 4. Linear regression coefficients of M_{BH} as a function of the bulge property x , starting from the top of column (1): bulge $3.6 \mu\text{m}$ luminosity (equation 3) compared with previous works and with K and V band results; bulge dynamical (equation 5) and stellar (equation 8) masses; bulge velocity dispersion (equation 9) and effective radius (equation 10). The coefficients are obtained using the normalizations in column (2) and with the methods listed in column (3). † G09 use a generalized maximum likelihood method to account for upper limits. Columns (4)-(6) list the intercept, slope and rms (in dex) respectively. We compare our results with the works listed in column (7). ‡ Lauer et al. (2007). ^a Coefficients obtained cutting the sample on the basis of the sphere of influence argument for the M_{BH} estimates. ^b Coefficients obtained only for elliptical galaxies.

trace M/L with a low scatter. Moreover the extent of our FP to compact sizes, its tight dispersion valid for all Hubble types, and the agreement with the $3.6 \mu\text{m}$ FP observed for pure elliptical galaxies should guarantee a reliable estimate for the M/L of our bulges.

We assume that M_{dyn} in bulges is dominated by the stellar mass, with a negligible contribution of dark matter and gas (Drory, Bender & Hopp 2004; Padmanabhan et al. 2004). We then consider our sample of spheroids (49 sources, see Tab.2) and fit a linear relation to M_{dyn} , computed as in equation (4), vs $L_{3.6,\text{bul}}$ as:

$$\log M_{\text{dyn}} = (11.04 \pm 0.03) + (1.18 \pm 0.07) \times [\log(L_{3.6,\text{bul}}/L_{3.6,\odot}) - 11] [rms = 0.13 \pm 0.04] \quad (6)$$

This is determined using LINMIX_ERR and is very tight with $rms \sim 0.10$. A tight $M_{\text{dyn}}-L_{3.6,\text{bul}}$ relation is not unexpected as it is just a different way (i.e. $\sigma^2 R_e$ vs $L_{3.6,\text{bul}}$) to express the FP. The $M_{\text{dyn}}-L_{3.6,\text{bul}}$ relation is shown in Fig. 4.

We now include a color correction to test how it affects the M/L ratio. Only 25 sources are included in this exercise, i.e. those whose classical bulges having V- and K-

magnitudes available in the literature (listed in Tab. 2). This allows a comparison with the above calibration and the following multi-linear regression:

$$\log M_{\text{dyn}} = (11.00 \pm 0.05) + (1.35 \pm 0.11) \times [\log(L_{3.6,\text{bul}}/L_{3.6,\odot}) - 11] + (0.07 \pm 0.10) \times [(V - K) - 2.54] [rms = 0.11 \pm 0.06] \quad (7)$$

where we add V-K color correction relative to the sample mean V-K color. The fit was performed using the multivariate extension of LINMIX_ERR (MLINMIX_ERR, Kelly 2007). The zeropoints and slopes of $L_{3.6,\text{bul}}$ in equation (6) and (7) are the same, as well as intrinsic dispersions, while the slope of $(V - K)$ is consistent with zero within the errors. This, clearly indicates that M/L for bulges is not affected by the V-K color and the $3.6 \mu\text{m}$ waveband is confirmed to be a better tracer of the stellar light than the K-band for both old and young stellar populations. With the $M_{\text{dyn}}-L_{3.6,\text{bul}}$ relation we have (i) calibrated the M/L ratio for the bulge component independently of the Hubble type of our galaxies, (ii) demonstrated how the $3.6 \mu\text{m}$ passband traces the stellar bulge mass better than optical or near-infrared colors for both young and old stellar popu-

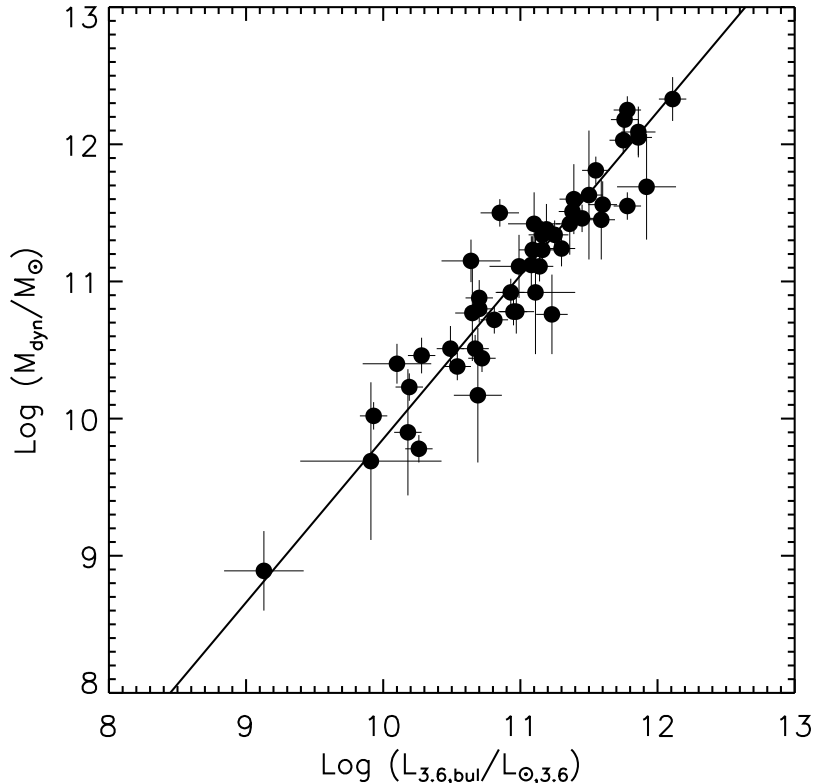


Figure 4. M_{dyn} versus $L_{3.6,\text{bul}}$. The black line represents the linear regression of equation (6).

lations, and finally (iii) found that V- and K- colors do not strongly influence M_* determinations based on $L_{3.6,\text{bul}}$.

Figure 3B shows the $M_{\text{BH}}-M_*$ linear regressions:

$$\begin{aligned} \log M_{\text{BH}}/M_{\odot} &= (8.16 \pm 0.06) + \\ & (0.79 \pm 0.08) \times [\log(M_*/M_{\odot}) - 11] \\ & [rms = 0.38 \pm 0.05] \end{aligned} \quad (8)$$

where we use equation (6) to calibrate M_* . Equation (8) is just the $M_{\text{BH}}-L_{3.6,\text{bul}}$ relation rescaled using equation (6) to determine M_* , in order to obtain a relation where M_* is derived by the host luminosity as done in studies at high redshifts (e.g. Merloni et al. 2010). Thus the black hole vs bulge mass correlation can be used as the reference scaling relation in the local Universe to probe a possible evolution of $M_{\text{BH}}-M_*$. This issue is discussed in Section 4. The coefficients and rms of equation (8) are consistent within the errors with the $M_{\text{BH}}-M_{\text{dyn}}$ scaling relation (for our choice fitting method, see equation (5), and Tab. 4). H09 find a steeper slope, but the use of an extinction corrected B-V color to calibrate M/L in the K band possibly affect the resulting $M_{\text{BH}}-M_*$. The M/L calibration presented here provide a robust estimate for M_* ; this issue is pursued further in Section 4.

3.3 A comparison with the $M_{\text{BH}}-\sigma$ relation

In the previous sections we have analyzed all the M_{BH} -bulge scaling relations which can be obtained using re-

sults from our bi-dimensional decomposition. We found (i) the same intrinsic dispersion for all the scaling relations $rms \sim 0.35$ dex, and (ii) that pseudobulges have a bimodal distribution with half of them lying on the relations within the observed scatter, while those harboring smaller BHs ($M_{\text{BH}} \leq 10^7 M_{\odot}$) significantly deviate from the regression. Here we compare our M_{BH} -bulge relations with $M_{\text{BH}}-\sigma$. A detailed analysis of the $M_{\text{BH}}-\sigma$ relation is beyond the scope of this paper, our aim is just to obtain a consistent comparison of $M_{\text{BH}}-\sigma$ with the other relations in terms of samples and fitting method. The classical bulges lie on the following correlation:

$$\begin{aligned} \log M_{\text{BH}} &= (8.29 \pm 0.05) + \\ & (4.0 \pm 0.4) \times \log(\sigma/200 \text{ km s}^{-1}) \\ & [rms = 0.33 \pm 0.04] \end{aligned} \quad (9)$$

In equation (9) the velocity dispersion is normalized at 200 km/s according to T02, G09. Figure 5 displays M_{BH} as a function of σ and the three linear regressions, with the parameters in Tab. 4.

Although the samples do not fully overlap, our BCES and FITEXY results are in good agreement with G09 and T02. More interesting is the correspondence, within the errors, between the $M_{\text{BH}}-M_{\text{dyn}}$ (M_* , $L_{3.6,\text{bul}}$) and $M_{\text{BH}}-\sigma$ intrinsic scatters ($rms \sim 0.3-0.35$ dex). Thus at 3.6 μm is not possible to assess whether the bulge dynamics or luminosity drive the observed scaling relations.

As expected, some, but not all, the pseudobulges are

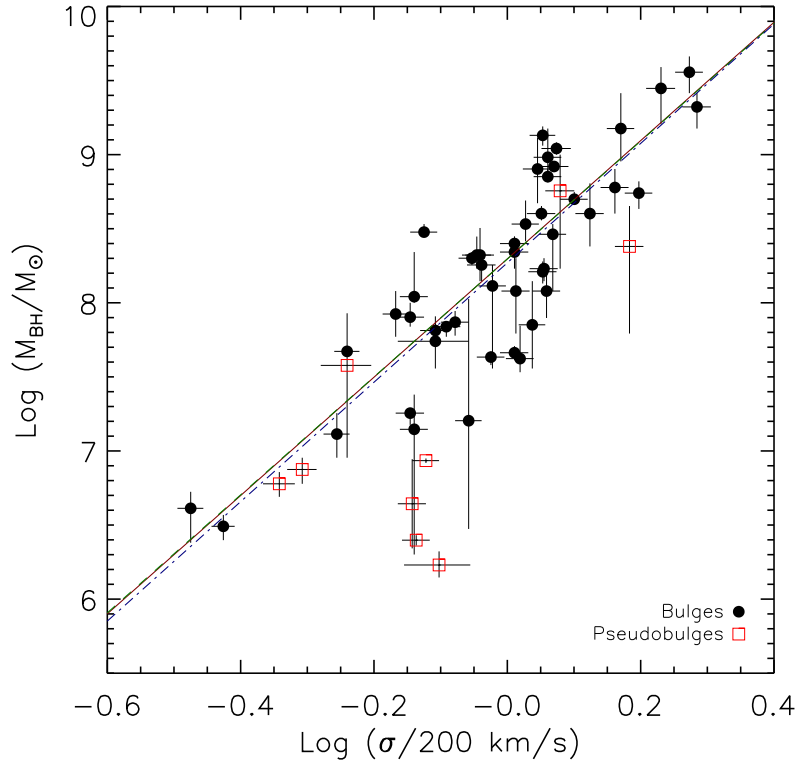


Figure 5. Scaling relations. The M_{BH} is plotted as a function of velocity dispersion. The linear regressions and symbols are as in Fig. 2.

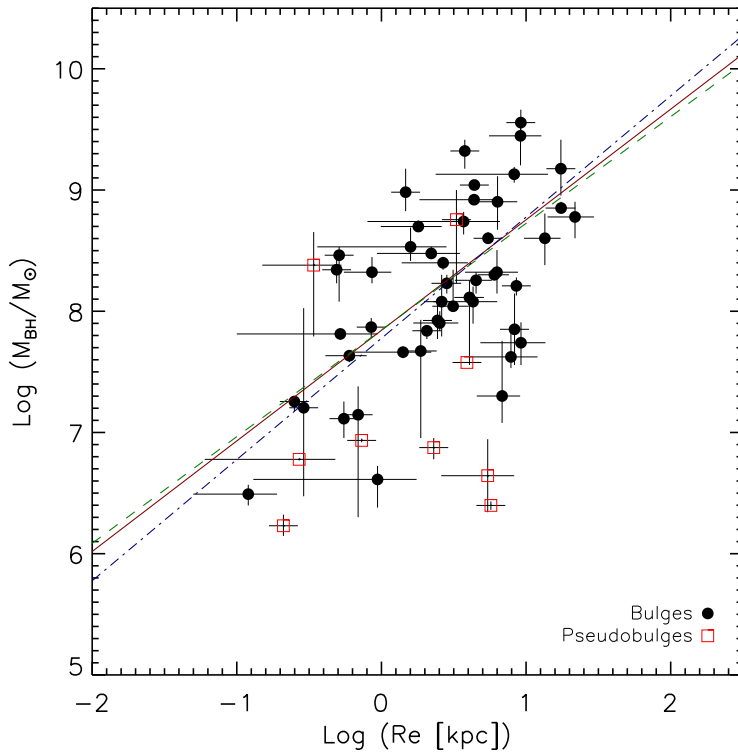


Figure 6. Scaling relations. The M_{BH} is plotted as a function of the bulge effective radius R_e . The linear regressions and symbols are as in Fig. 2.

displaced from the inferred regressions. These are CIRCI-NUS, IC2560, NGC1068, NGC3079 and NGC3998; therefore there is a good overlap (4/6 where the exceptions are NGC3368 and NGC3998) with the deviant pseudobulges found in the previous sections. This discrepancy, also found in H09 and Nowak et al. 2010, could arise from several different causes; there could be an additional nuclear component not identified with our image 2D decomposition; or e. g. pseudobulges could have a different evolutionary history than classical bulges. We defer a detailed discussion to the following section.

3.4 M_{BH} versus R_e , the effective radius at $3.6 \mu\text{m}$

M_{BH} has been observed to be separately related to the bulge stellar velocity dispersion σ and its effective radius R_e . This has been first observed in MH03 by a partial correlation analysis. Figure 6 shows the $M_{\text{BH}}-R_e$ relation obtained with our $3.6 \mu\text{m}$ 2D decomposition, where the LINMIX ERR method gives:

$$\begin{aligned} \log M_{\text{BH}} = & (8.22 \pm 0.08) + \\ & (0.88 \pm 0.17) \times [\log(R_e/kpc) - 0.4] \\ & [rms = 0.54 \pm 0.07] \end{aligned} \quad (10)$$

The three linear regression in Tab. 4 are in good agreement within the errors. The intrinsic dispersion is significantly larger than in other relations. Nevertheless the possible existence of $M_{\text{BH}}-R_e$ is intriguing and prompts investigation of a possible fundamental plane for BHs, in analogy with the galaxies FP.

It is still unclear whether *one* M_{BH} -bulge relation is significantly tighter than the others. Hopkins et al. (2007) explained the lack of a dominant M_{BH} -bulge scaling relation because each of them is the projection of the same fundamental plane relating M_{BH} with two or more bulge properties. However, the issue of a BH fundamental plane is still matter of debate: Graham 2008a showed that the need for a M_{BH} fundamental plane originates on a displacement of barred galaxies with respect to the residuals of the $M_{\text{BH}}-\sigma$ relation.

If a M_{BH} FP actually exists, it should be easily observed at $3.6 \mu\text{m}$. Thus here we follow MH03 and Graham (2008a) and compare the residuals of $M_{\text{BH}}-\sigma$ for our bulges (expressed in equation 9) with the effective radius (column 4 in Tab. 3). Figure 7 shows this comparison where we highlight the position of barred galaxies and pseudobulges. Hence, we check for a possible significant correlation performing both the Pearson and Spearman rank correlation test. As shown in Tab.5, there is *no* significant correlation either for the entire sample or excluding barred galaxies and/or pseudobulges. Thus, our analysis at $3.6 \mu\text{m}$ does not confirm the existence of BH FP. We refer to a forthcoming paper (Marconi et al. 2011 in prep.) for a detailed study of the origin of the FP for supermassive BHs.

4 DISCUSSION

The high signal-to-noise images provided by *Spitzer*/IRAC and our improved 2D analysis have allowed us to obtain

accurate estimates of bulge luminosities and effective radii at $3.6 \mu\text{m}$, as demonstrated by the tight fundamental plane and $M_{\text{dyn}}-L_{\text{bul}}$ relations. We have been able to (i) calibrate the $M_{\star}-L_{\text{bul}}$ relation, accurate to 0.10 ± 0.05 rms without any color correction and (ii) securely define pseudobulges through the Sérsic index value ($n \leq 2$) and study their location with respect to the scaling relations for classical bulges. We have then obtained the M_{BH} -galaxy relations for classical bulges using our photometry at $3.6 \mu\text{m}$. They are expressed in Eqs. 3, 5, and 8, and shown in Figs. 2, 3 and 5.

All the above scaling relations have an intrinsic dispersion of 0.35 dex (from a Bayesian approach to linear regression, see Tab.4) and are in perfect agreement with the $M_{\text{BH}}-\sigma$ relation for our galaxies in equation (9). Considering the methods adopted in literature to perform linear regressions that account for the intrinsic scatter (BCES and FITEXY) our $3.6 \mu\text{m}$ correlations are as tight as the M_{BH} -bulge K-band luminosity (MH03, H09) and tighter than in V-band (G09). Moreover the $M_{\text{BH}}-M_{\text{dyn}}$ and $M_{\text{BH}}-M_{\star}$ agree very well with MH03, HR04 and H09, with the new advantage of an accurate M/L relation for bulges at $3.6 \mu\text{m}$ calibrated without any color correction.

Figure 3 present the $M_{\text{BH}}-M_{\star}$ relation, where M_{\star} is obtained by combining L_{bul} with our calibrated $M_{\star}-L_{\text{bul}}$ relation. This relation represents the reference $M_{\text{BH}}-M_{\star}$ in the local Universe for studies of the M_{BH} -galaxy scaling relations at higher z , based on M_{\star} derived from luminosity measurements (Merloni et al. 2010, Trakhtenbrot & Netzer 2010). The z evolution of M_{BH} -galaxy scaling relations has been studied in several papers but remains controversial. For instance, Woo et al. (2008) report a significant evolution of the BH-bulge relations at $z = 0.3 - 0.6$, with larger BH masses for given bulge σ /luminosity with respect to local values. This evolution is however not found by Labita et al. (2009) or Shen et al. (2008). Shields et al. (2003) find no evolution of $M_{\text{BH}}-\sigma$ up to $z \sim 2$ but using [OIII] line width as a surrogate for σ . Indeed, at high redshift a dynamical measurement of the bulge mass based on σ is difficult due to the limited signal-to-noise and spatial resolution. On the contrary the total stellar mass of the host galaxy is relatively easier to estimate from host galaxy luminosities and colors (e.g. Peng et al. 2006), or by deconvolving AGN and galaxy spectral energy distributions (Merloni et al. 2010) or by applying the correlation between the AGN bolometric luminosity and M_{BH} together with the relation between the star formation rate and M_{\star} in star forming galaxies (Trakhtenbrot & Netzer 2010). The above observational works suggest that the M_{BH}/M_{\star} at high redshift is significantly higher than the local value. In any case, observations at high redshifts are fundamental to constrain models of BH-galaxy co-evolution and to probe different paths followed by galaxies during their evolution and the building up of the M_{BH} -bulge relations (Lamastra et al. 2010 and references therein).

In Section 3.2, the tight $M_{\text{dyn}}-L_{3.6, \text{bul}}$ relation with negligible color corrections justifies the validity of 2D decomposition to measure M/L at $3.6 \mu\text{m}$. This (i) unveils the capability of our $M_{\text{BH}}-M_{\text{dyn}}$ (and thus M_{\star}) to be a suitable benchmark to probe the M_{BH} -bulge co-evolution and to constrain theoretical models. In fact, in the next decade the instruments onboard the *James Webb Space Telescope* (JWST) will increase the possibility to further explore with unprecedented accuracy this waveband.

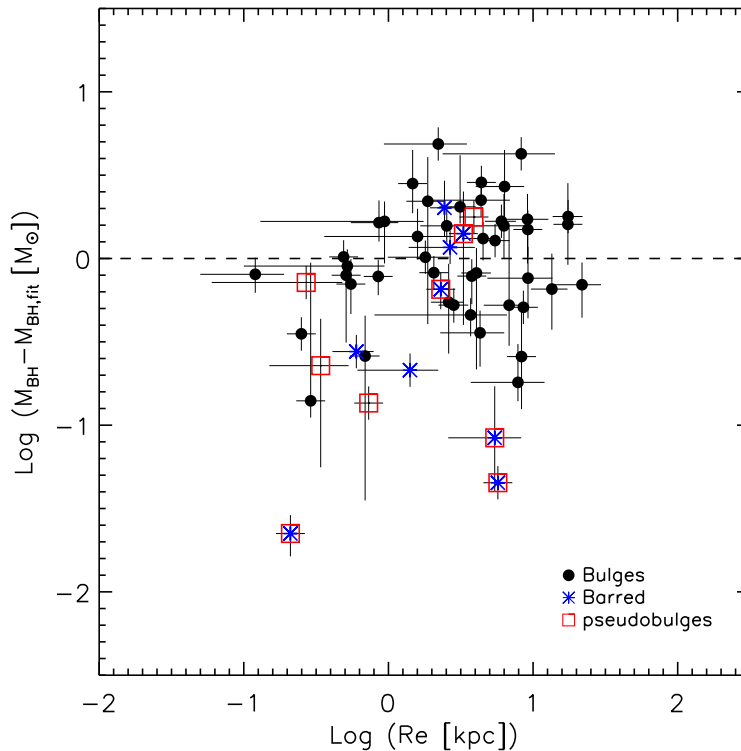


Figure 7. M_{BH} (in Tab.2) residuals about their $M_{\text{BH}}-\sigma$ relation (Eq 9) versus R_e . The dashed line represents null residuals. Black points are early- and late- type galaxies, blue asterisks are barred galaxies and open red squares are pseudobulges.

STATISTICAL TESTS FOR M_{BH} RESIDUALS

Sample	Test	ρ	significance
all galaxies	Spearman	0.22	0.10
	Pearson	0.29	-
no barred	Spearman	0.21	0.16
	Pearson	0.29	-
no pseudobulges	Spearman	0.16	0.26
	Pearson	0.24	-
no pseudobulges, no bar	Spearman	0.11	0.48
	Pearson	0.20	-

Table 5. Statistical test for the M_{BH} residuals about their $M_{\text{BH}}-\sigma$ correlation with R_e in Fig. 7. Column 1: tests are performed for the total sample and sub-samples excluding barred galaxies and pseudobulges. Column 2: the kind of statistic applied to data (Spearman rank correlation and Pearson correlation). Column 3: correlation coefficient ρ . Column 4: and the two-sided significance of ρ deviation from zero in the Spearman rank correlation. The significance is a value in the interval $[0.0, 1.0]$; a value consistent with zero indicates a significant correlation.

The other (ii) intriguing result found here is related to the behavior of pseudobulges. The displacement of pseudobulges, located below the scaling relations, is reported in H09 and Nowak et al. (2010). In §2.4 we followed FD10 and identified 9 pseudobulges with Sérsic index $n \leq 2$. Of these, CIRCINUS, IC2560, NGC1068, and NGC3398 lie below *all* the M_{BH} scaling relations; NGC3368 deviates from $M_{\text{BH}}-L_{3.6,\text{bul}}$, $-M_{\text{dyn}}$ but not from $M_{\text{BH}}-\sigma$, while the contrary happens for NGC3998. The other pseudobulges NGC3489,

NGC4258, NGC4374, NGC4594 are within the observed scatter. As mentioned in §3.3 this discrepancy can arise from several causes. We first note that the $n \leq 2$ is a statistical property of pseudobulges; indeed the tails of the Sérsic index distributions for classical and pseudobulges overlaps around $n \sim 2$ (see Fig. 9 in Fisher & Drory 2008 and FD10). Thus, not all bulges with a low n would be actual pseudobulges from the dynamical point of view (Gadotti 2009).

Anyway, it is interesting to explore the possible expla-

nations once we assume that all the nine galaxies actually harbor a pseudobulge.

(1) Additional nuclear component on small scales ($\simeq 10$ arcsec), such as bars, ovals and lenses are observed not only in disks but also in S0 galaxies (Laurikainen et al. 2009). With the grid method applied for 2D fitting (see §2.3), an additional component on small image scales of 10-15 pixels can not be taken into account, because (a) it is difficult to constrain input parameters while automatically running the fits, and (b) the model does not require any additional component to match our quality criteria (see §2.3).

(2) Nowak et al. (2010) define NGC3368 and NGC3489 as pseudobulges by resolving the nuclear dynamics, and find the coexistence of a classical bulge with a pseudobulge, where the M_{BH} seems to better correlate with the classical bulge alone. For the same reasons outlined above, it is beyond the possibilities of our analysis to deconvolve the classical bulge from the pseudobulge component.

(3) The nine pseudobulges could be in different evolutionary stages. Montecarlo simulations in Lamastra et al. (2010) show how in the buildup of the local $M_{\text{BH}}-M_{\star}$ relation, galaxies can follow various evolutionary paths that proceed from below the correlation and reach their final position passing above it. Thus, the position of each source could just be the result of the different evolutionary paths being followed.

(4) Finally, nuclear star clusters (NSCs) may be common in those spheroid with $M_{\star} \sim 10^8 - 10^{11} M_{\odot}$ harboring a $M_{\text{BH}} < 10^7 M_{\odot}$, and may contribute significantly at the mass of the central object increasing its value of a factor of ~ 2 (Graham & Spitler 2009 and references therein). A larger value of M_{BH} can prevent the coexistence of a NSC, because the very central stars should be either disrupted by the BH gravity or kicked away by tidal forces. Moreover Graham & Spitler (2009) derive a linear regression between the nuclear mass (BH plus NSC) and the stellar mass of the host spheroid. Thus, the proper quantity to be plotted on the y-axis seems to be M_{BH} plus the NSC mass, at least for $M_{\text{BH}} < 10^7 M_{\odot}$. The identification of NSCs requires the highest spatial resolutions available with the current instrumentation and can not be reached with *Spitzer* even for the closest of our sources.

We conclude that the observed displacement of pseudobulges could arise from observational limitations, true evolution, or a combination of the two.

5 CONCLUSIONS

In this work we have investigated the scaling relations observed in the local Universe between M_{BH} and the structural parameters of the host bulges. The analysis is based on a 2D decomposition of $3.6 \mu\text{m}$ *Spitzer*/IRAC images of 57 early- and late- type galaxies with M_{BH} measurements. Given the well known degeneracy between the bulge Sérsic index n and effective radius R_e , we have adopted a grid-method to fit IRAC images and determine n rather than let it freely vary. The accuracy of our analysis is verified by the agreement of our bulges with the mid-infrared fundamental plane determination by JI08. Our galaxies extend their $3.6 \mu\text{m}$ FP by doubling the R_e range towards smaller radii and none of our galaxies deviate significantly from the JI08 FP. This al-

lows us to reliably (i) calibrate M/L at $3.6 \mu\text{m}$, (ii) study the M_{BH} - scaling relation and (iii) identify pseudobulges in our sample.

We obtained a tight ($rms = 0.10$ dex) $M_{\text{dyn}}-L_{3.6,\text{bul}}$ relation:

$$\log M_{\text{dyn}}/M_{\odot} = 11.04 + 1.18 \times [\log(L_{3.6,\text{bul}}/L_{3.6,\odot}) - 11],$$

which allows us to estimate stellar masses based on luminosities at $3.6 \mu\text{m}$ with high accuracy. The $3.6 \mu\text{m}$ luminosity appears to be the best tracer of M_{\star} yet found.

The relations between M_{BH} , luminosity, masses, and effective radius, fitted with a Bayesian approach to linear regression are:

$$\log M_{\text{BH}}/M_{\odot} = 8.19 + 0.93 \times [\log(L_{3.6,\text{bul}}/L_{3.6,\odot}) - 11],$$

$$\log M_{\text{BH}}/M_{\odot} = 8.20 + 0.79 \times [\log(M_{\text{dyn}}/M_{\odot}) - 11],$$

$$\log M_{\text{BH}}/M_{\odot} = 8.16 + 0.79 \times [\log(M_{\star}/M_{\odot}) - 11],$$

$$\log M_{\text{BH}}/M_{\odot} = 8.22 + 0.9 \times [\log(R_e/kpc) - 0.4],$$

all with the same intrinsic dispersion of $rms \sim 0.35$ dex except for $M_{\text{BH}}-R_e$ which has $rms \sim 0.5$ dex. Our $M_{\text{BH}}-M_{\star}$ relation can be used as the local reference for high redshift studies which probe the cosmic evolution of M_{BH} -galaxy scaling relations.

These $3.6 \mu\text{m}$ $M_{\text{BH}}-L_{3.6,\text{bul}}$, $M_{\text{BH}}-M_{\text{dyn}}$, $M_{\text{BH}}-M_{\star}$ relations turn out to be as tight as $M_{\text{BH}}-\sigma$ and, moreover, they are consistent with previous determinations from the literature at shorter wavelengths.

We independently identified as pseudobulges those galaxies with Sérsic index lower than 2 and found 9 sources that satisfy this criterion. Of these, 4 pseudobulges lie on scaling relations within the observed scatter, while those with M_{BH} lower than $10^7 M_{\odot}$ are significantly displaced. We discussed the different physical and evolutionary origins for such behavior, while considering the presence of nuclear morphological components not reproduced by our two-dimensional decomposition.

Finally, we verified the existence of a possible FP for supermassive BHs, relating M_{BH} with two or more bulge properties. We did not find any correlation between the residuals of $M_{\text{BH}}-\sigma$ and the effective radius, showing that our data do not require the existence of any BH fundamental plane.

6 ACKNOWLEDGMENTS

The authors are grateful to the anonymous referee for the constructive comments and suggestions. We acknowledge B. M. Peterson for discussing the background effects and analysis method. E. Sani thanks R. I. Davies, A. W. Graham, and N. Neumayer for precious discussions on the pseudobulges and barred galaxies behaviors. This work has been partially supported by the NASA grants *Spitzer*/1343503 and GO-11735.01. We acknowledge the usage of the HyperLeda database (<http://leda.univ-lyon1.fr>). This research has made use of the NASA/IPAC extragalactic database (NED).

REFERENCES

Akritas M. G., Bershady M. A., 1996, *ApJ*, 470, 706

- Allen C. W., 1976, *Astrophysical Quantities*. Athlone, London
- Aller M. C., Richstone D. O., 2007, *ApJ*, 665, 120
- Andredakis Y. C., Peletier R. F., Balcells M., 1995, *MNRAS*, 275, 874
- Barway S., Kembhavi A., 2007, *ApJ*, 662, L67
- Batcheldor D., 2010, *ApJ*, 711, L108
- Bell E. F., de Jong R. S., 2001, *ApJ*, 550, 212
- Bell E. F., McIntosh D. H., Katz N., Weinberg M. D., 2003, *ApJS*, 149, 289
- Bessell M. S., & Brett J. M. 1988, *PASP*, 100, 1134
- Burstein D., Bender R., Faber S., Nolthenius R., 1997, *AJ*, 114, 1365
- Capellari M., et al. 2006, *MNRAS*, 366, 1126
- Drory N., Bender R., Hopp U., 2004, *ApJ*, 616, L103
- de Souza R. E., Gadotti D. A., dos Anjos S., 2004, *ApJS*, 153, 411
- Djorgovski S., Davis M., 1987, *ApJ*, 313, 59
- Erwin P. 2010, arXiv:1002.1445
- Fazio G. G., et al. 2004, *Bulletin of the American Astronomical Society*, 36, 699
- Feoli A., Mancini L., Marulli F., van den Bergh S., 2010, *GRGr*, 57
- Ferrarese L., & Merritt D. 2000, *ApJ*, 539, L9
- Fisher D. B., & Drory N. 2008, *AJ*, 136, 773
- Fisher D. B., & Drory N. 2010, *ApJ*, 716, 942
- Gadotti D. A. 2009, *MNRAS*, 393, 1531
- Gebhardt K., et al. 2000, *ApJ*, 539, L13
- Gebhardt K., et al., 2003, *ApJ*, 583, 92
- Giovanardi C., Hunt L. K., 1988, *AJ*, 95, 408
- Graham, A. W. 2007, *MNRAS*, 379, 711
- Graham A. W. 2008a, *Publications of the Astronomical Society of Australia*, 25, 167
- Graham A. W., 2008b, *ApJ*, 680, 143
- Graham A. W., Li I.-h., 2009, *ApJ*, 698, 812
- Graham A. W., & Spitler L. R. 2009, *MNRAS*, 397, 2148
- Greene J. E., Ho L. C., & Barth A. J. 2008, *ApJ*, 688, 159
- Gültekin K., et al. 2009, *ApJ*, 698, 198
- Häring N., & Rix H.-W. 2004, *ApJ*, 604, L89
- Helou G., et al., 2004, *ApJS*, 154, 253
- Hopkins P. F., Hernquist L., Cox T. J., Robertson B., & Krause E. 2007, *ApJ*, 669, 67
- Hu J. 2009, arXiv:0908.2028
- Hunt L. K., Pierini D., & Giovanardi C. 2004, *A&A*, 414, 905
- Kelly B. C. 2007, *ApJ*, 665, 1489
- Kormendy J., & Richstone D. 1995, *ARA&A*, 33, 581
- Kormendy J., & Kennicutt R. C., Jr. 2004, *ARA&A*, 42, 603
- Jorgensen I., Franx M., Kjaergaard P., 1996, *MNRAS*, 280, 167
- Jun H. D., & Im M. 2008, *ApJ*, 678, L97
- Labita M., Decarli R., Treves A., Falomo R., 2009, *MNRAS*, 399, 2099
- Lamastra A., Menci N., Maiolino R., Fiore F., & Merloni A. 2010, *MNRAS*, 405, 29
- Leitherer C., et al., 1999, *ApJS*, 123, 3
- Lauer T. R., et al. 2007, *ApJ*, 662, 808
- Laurikainen E., Salo H., Buta R., & Knapen J. H. 2009, *ApJ*, 692, L34
- Magorrian J., et al., 1998, *AJ*, 115, 2285
- Merloni A., et al. 2010, *ApJ*, 708, 137
- Makovoz D., & Marleau F. R. 2005, *PASP*, 117, 1113
- Marconi A., & Hunt L. K. 2003, *ApJ*, 589, L21
- Marconi A., Risaliti G., Gilli R., Hunt L. K., Maiolino R., & Salvati, M. 2004, *MNRAS*, 351, 169
- Moriondo G., Giovanardi C., Hunt L. K., 1998, *A&AS*, 130, 81
- Nowak N., Thomas J., Erwin P., Saglia R. P., Bender R., Davies R. I., 2010, *MNRAS*, 403, 646
- Padmanabhan N., et al., 2004, *NewA*, 9, 329
- Peng C. Y., Ho L. C., Impey C. D., Rix H.-W., 2002, *AJ*, 124, 266
- Peng C. Y., Impey C. D., Rix H.-W., Kochanek C. S., Keeton C. R., Falco E. E., Lehár J., McLeod B. A., 2006, *ApJ*, 649, 616
- Peng C. Y., Ho L. C., Impey C. D., Rix H. W., 2007, *AAS*, 38, 804
- Prugniel P., Simien F., 1996, *A&A*, 309, 749
- Reach W. T., et al., 2005, *PASP*, 117, 978
- Shankar F., 2009, *NewAR*, 53, 57
- Shen Y., Greene J. E., Strauss M. A., Richards G. T., Schneider D. P., 2008, *ApJ*, 680, 169
- Shields G. A., Gebhardt K., Salviander S., Wills B. J., Xie B., Brotherton M. S., Yuan J., Dietrich M., 2003, *ApJ*, 583, 124
- Soltan A., 1982, *MNRAS*, 200, 115
- Trakhtenbrot B., & Netzer H. 2010, *MNRAS*, L76
- Tremaine S., et al. 2002, *ApJ*, 574, 740
- Woo J.-H., Treu T., Malkan M. A., Blandford R. D., 2008, *ApJ*, 681, 925

APPENDIX A: DETAILS OF THE 2D FITTING METHOD

An important issue for bulge decomposition is related to the fitting method. In the case of one dimensional fitting, radially averaged surface brightness profiles are fit with one or more components. Consequently, information related to, e.g., isophotal twists or changes in ellipticity is lost and the galaxy profile is poorly defined. Moreover, in one-dimensional fitting different morphological components may appear to merge smoothly, generating degeneracy and non-uniqueness in the profile decomposition. A two-dimensional analysis breaks this degeneracy (see, e.g., Peng et al. 2002, de Souza, Gadotti & dos Anjos 2004).

In Section 2.3 we describe in detail our grid method for a two-dimensional decomposition of *Spitzer*/IRAC 3.6 μm images. This is an improved version of the two-dimensional method commonly adopted in the literature, where all galaxy parameters are left free to vary. In fact, degeneracies also affect two dimensional methods: one is related to the functional form of the bulge profile, "Sérsic" profile, in which the n and R_e parameters are strongly coupled. Moreover, the fainter outer parts of galaxies may be affected by errors on background estimates. In Section 2.3 we also justify our choice of the best fit by a quantitative inspection of the χ^2 as a function of the radius. We note that the errors on the bulges parameters in Tab. 3 are *not* one standard deviation errors, rather are given by the discrepancy between the best fit values and the ones obtained from the model having the closest s , $s + \sigma_s$ or $s - \sigma_s$ value and the lowest possible reduced χ^2 within $R_{0.5}^{opt}$ according to the criteria described in Section 2.3. For each galaxy, Fig. A1 shows the image, 2D model, and residuals. It also shows the trend of χ^2 vs the source radius for: the best model (i.e. best n in red), the fit for the nearest n with low χ^2 within $R_{0.5}^{opt}$ maintaining the same sky values (in dark blue, is plotted to show the dependence on n at small radii), and the model from which we compute the absolute error on free parameters (in sky blue). Even with the above technique when real galaxies are fitted in two dimensions, their surface brightness in the circumnuclear regions is rarely well reproduced only by axisymmetric components. In fact, it is not uncommon to find inner disks and non-axisymmetric features in elliptical galaxies (e.g. Moriondo et al. 1998, Laurikainen et al. 2005). Substructure in the circumnuclear regions of both elliptical and spiral galaxies (such ovals, disks, lenses) occurs frequently, and is usually impossible to fit them with only axisymmetric components, with or without the addition of a bar. This is the origin of nuclear structures in the residual images shown in Fig. A1. Finally, we also note that our models (red curves in Fig. A1) do not require any additional nuclear component to respect the quality criteria of Section 2.3, for which, no more than 5% of the nuclear flux should be lost.

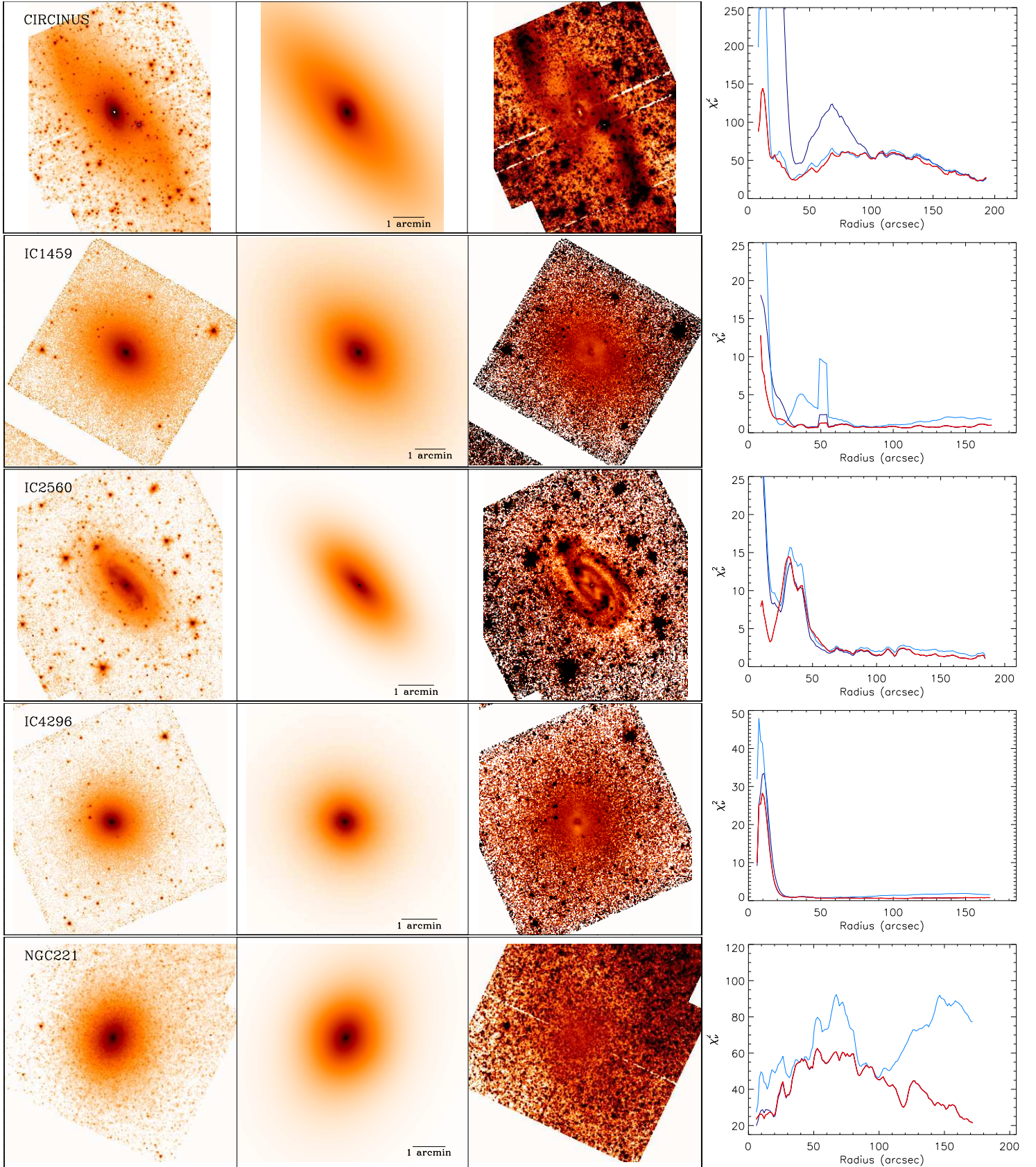


Figure A1. Two-dimensional decomposition. The image, best-fit model and residuals are shown in logarithmic scale. The residuals are stretched (± 0.25 dex) to highlight the finest details. On the right, the χ^2 is plotted as a function of the radius (in arcsec). Red: best model. Dark blue: the fit with closest n and the lowest χ^2 within $R_{0.5}^{\text{opt}}$. Light blue: same for the closest sky ($s \pm \sigma_s$, see Section 2.3 and Appendix A for details). A color version of this figure is available online.

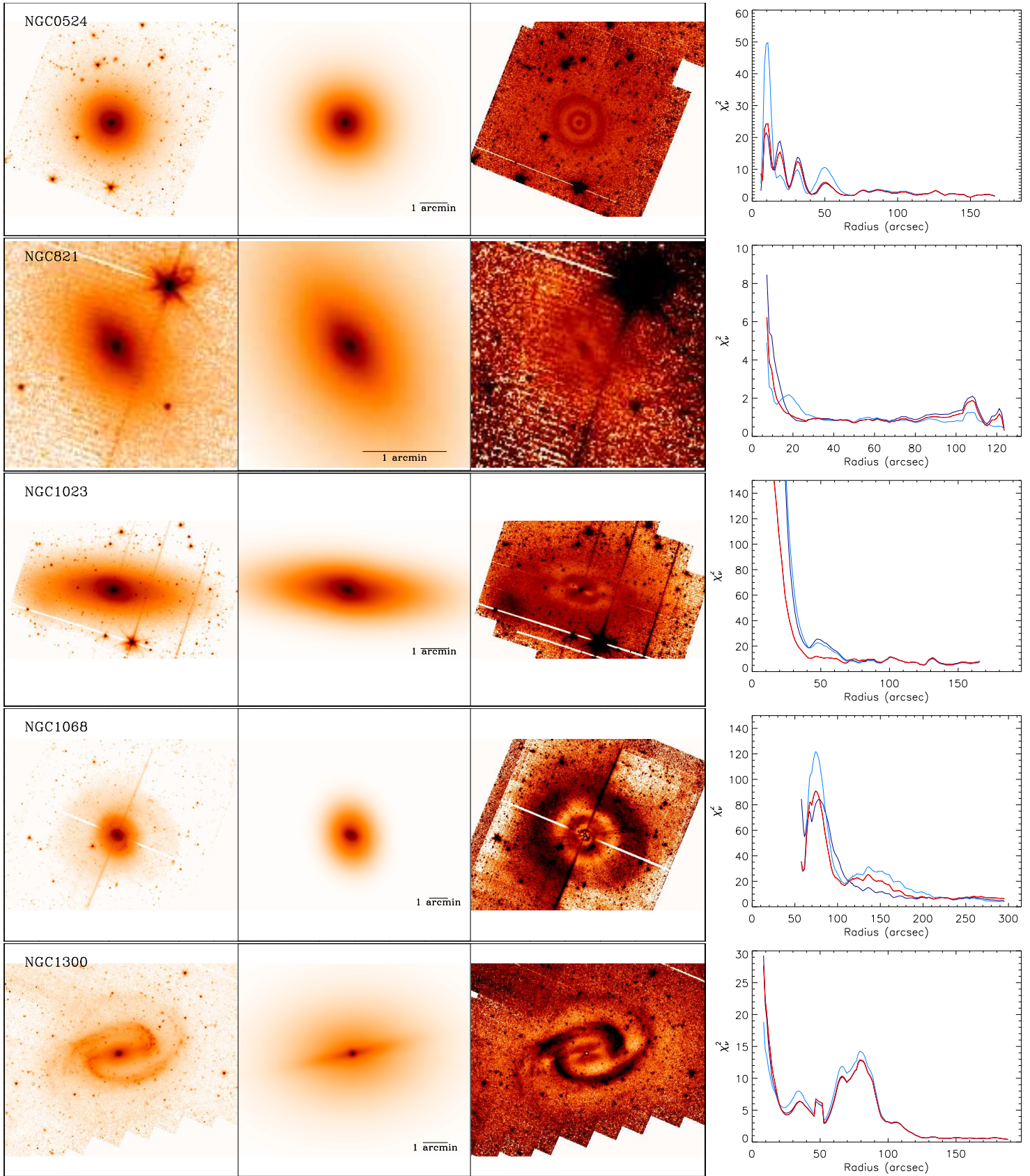


Figure A1. Continued.

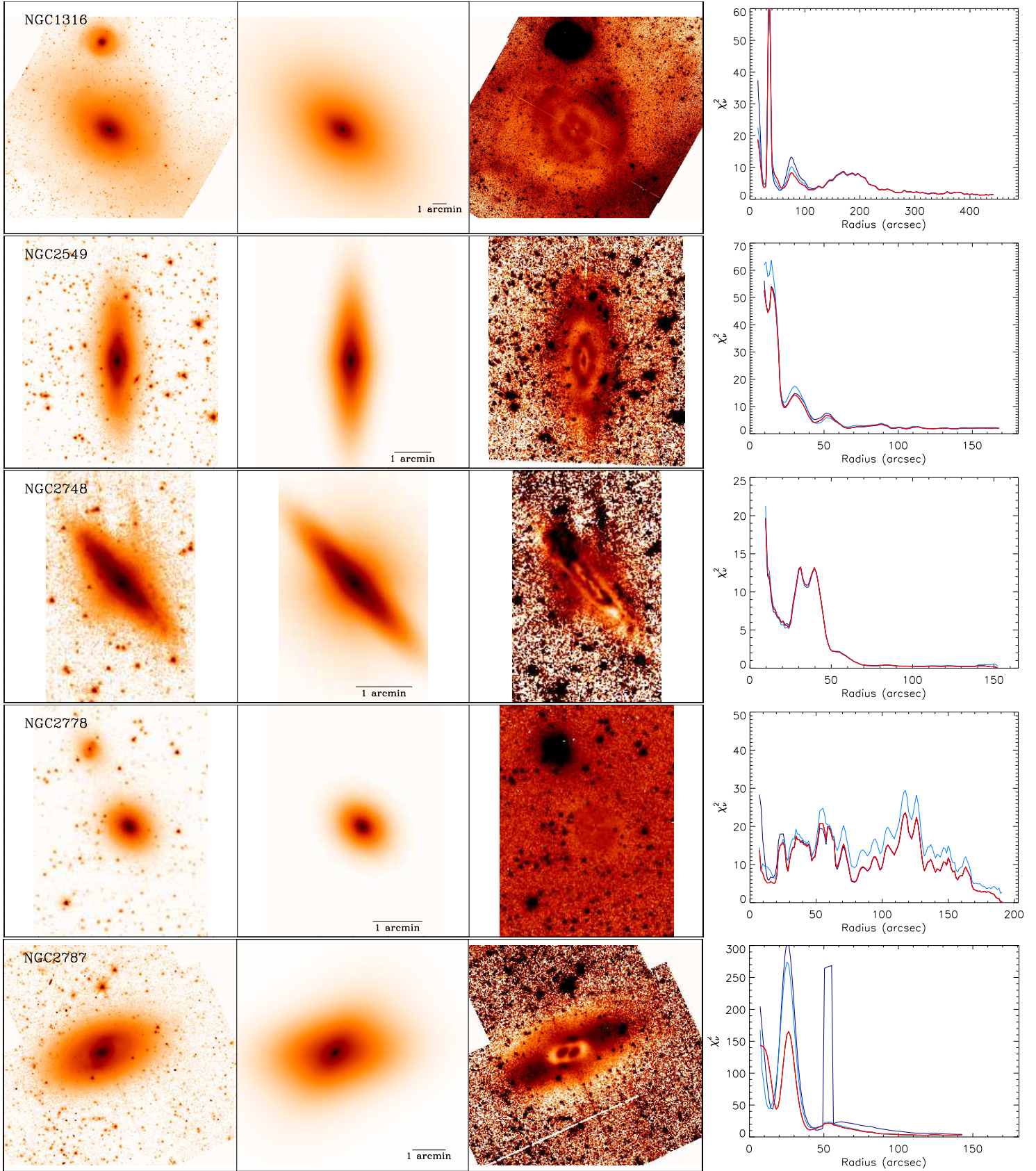


Figure A1. Continued.

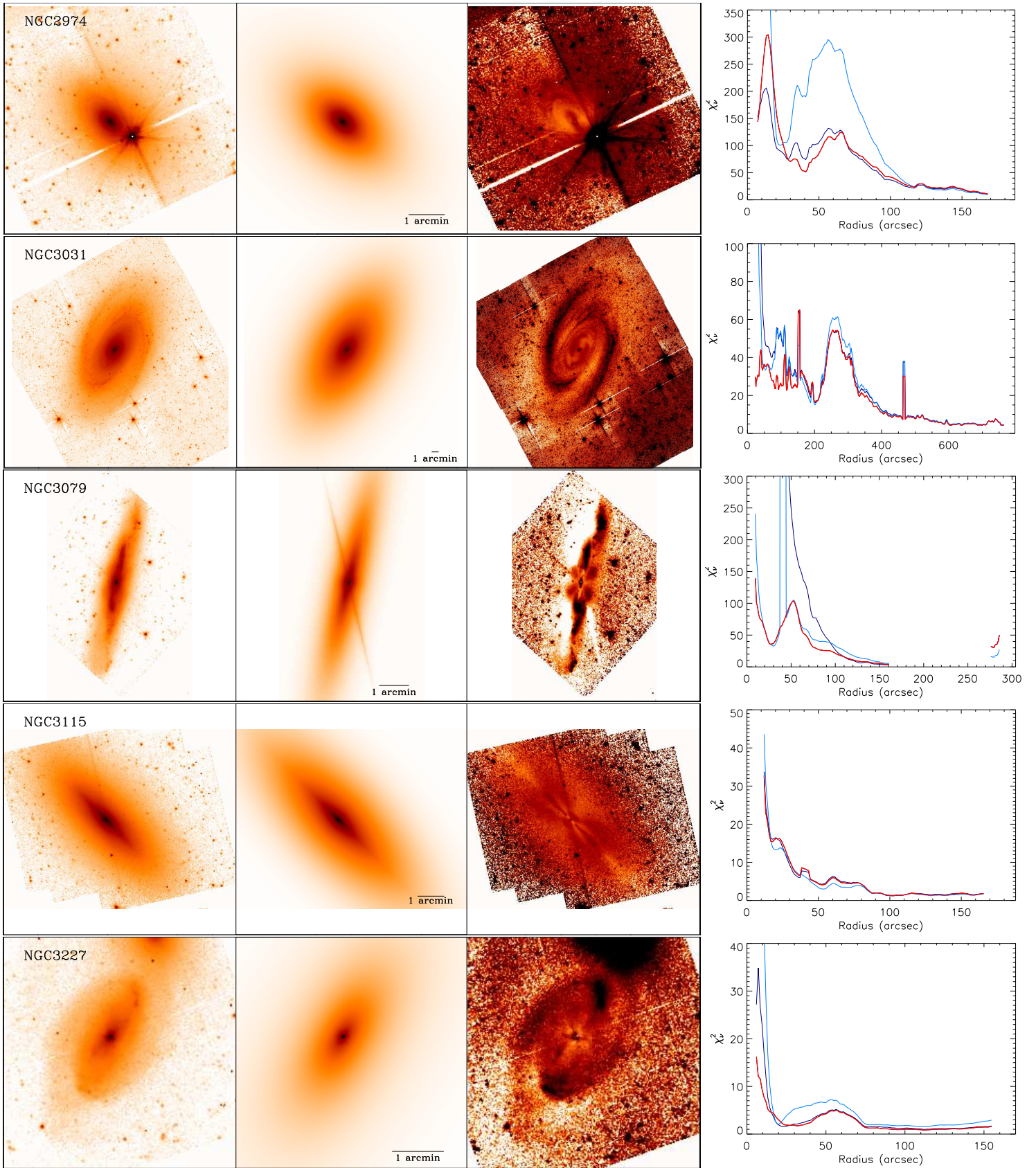


Figure A1. Continued.

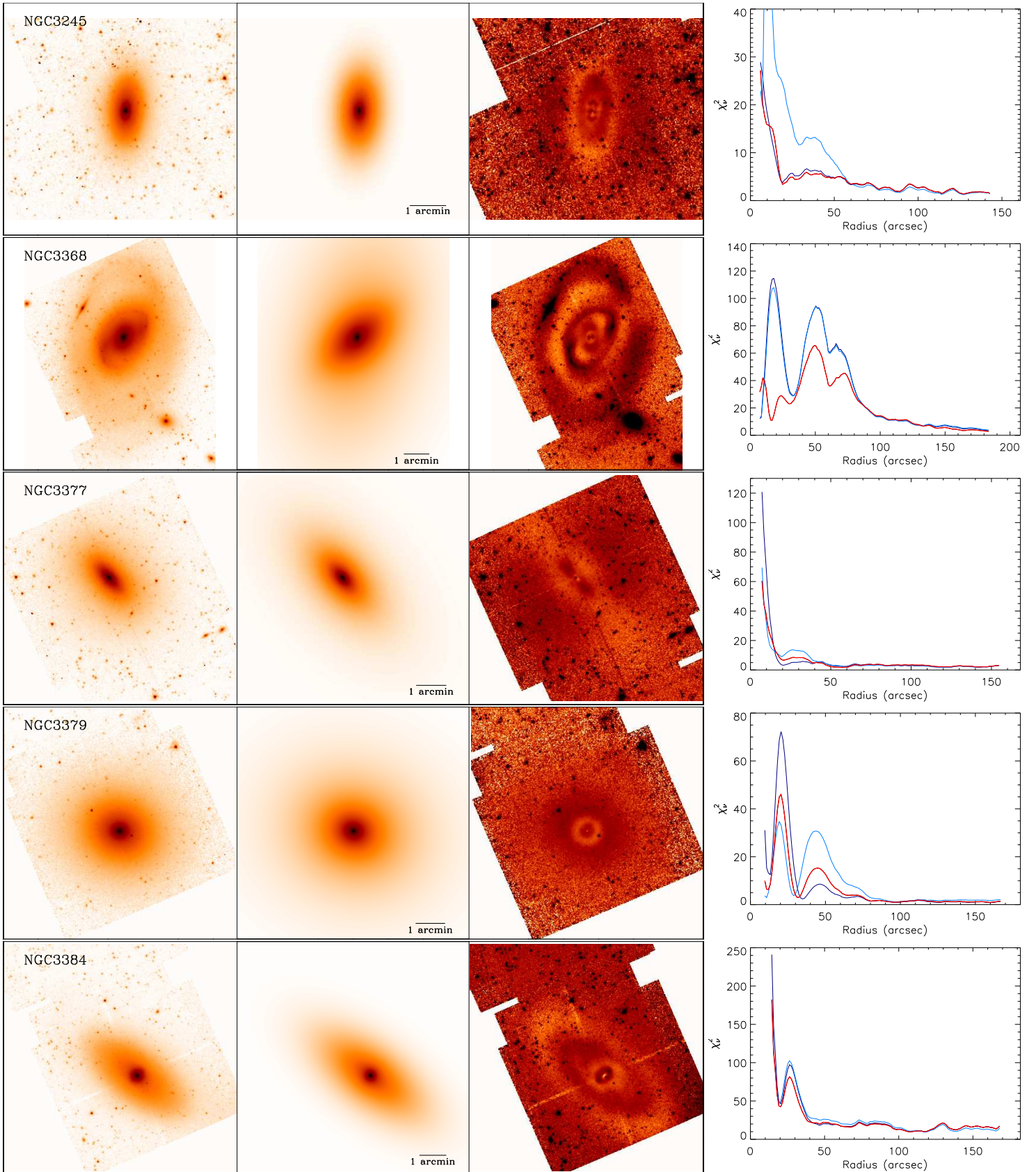


Figure A1. Continued.

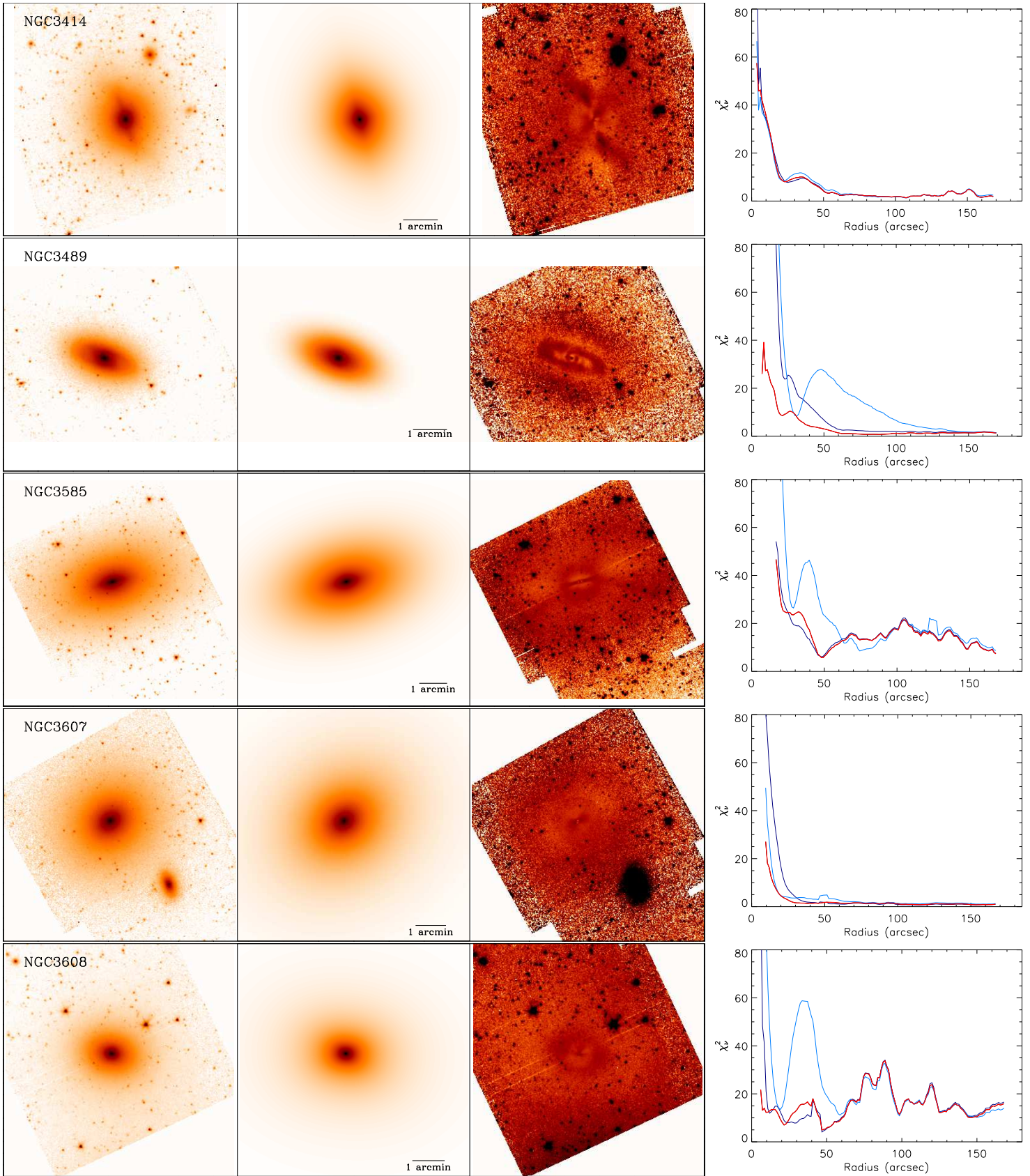


Figure A1. Continued.

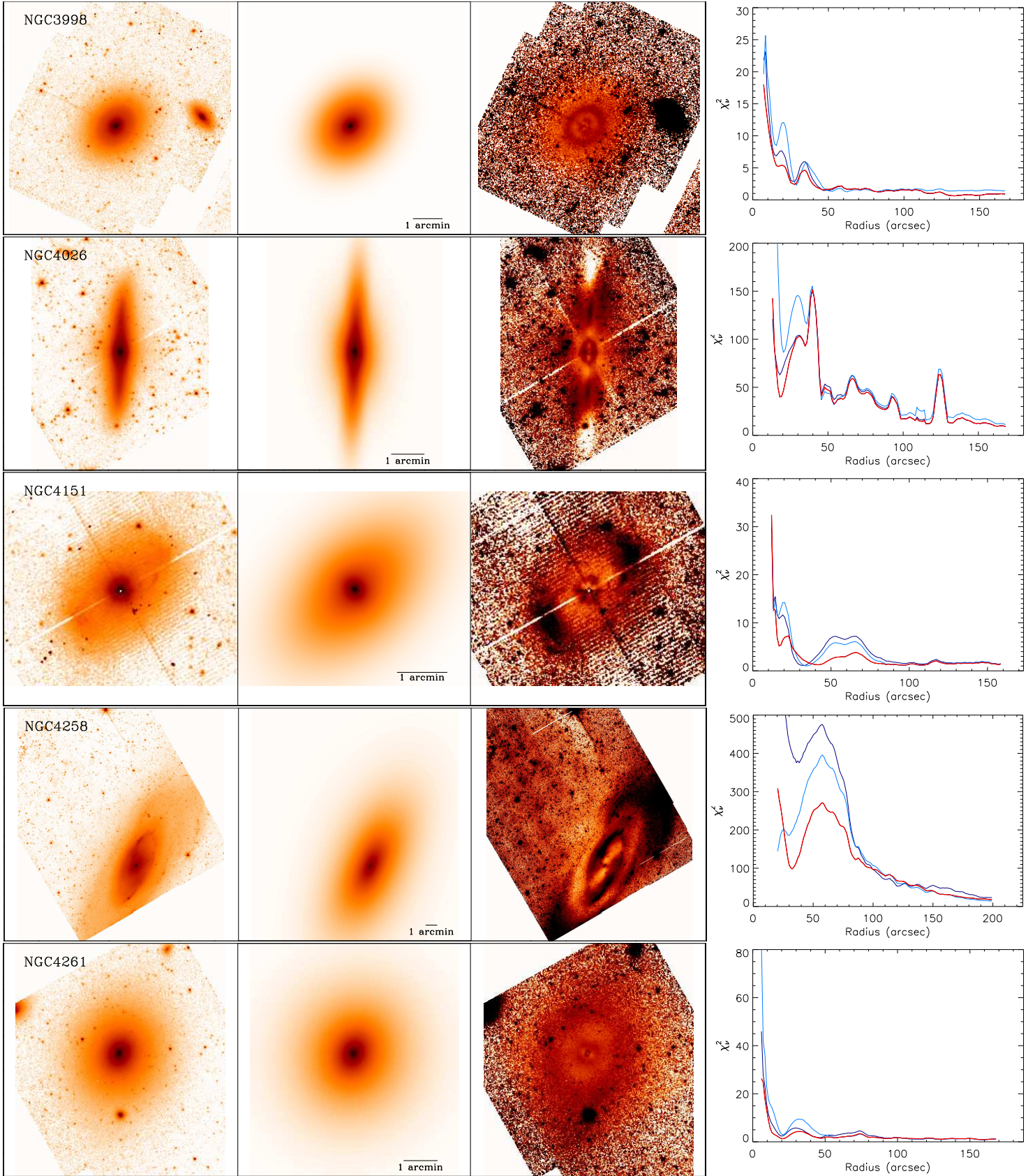


Figure A1. Continued.

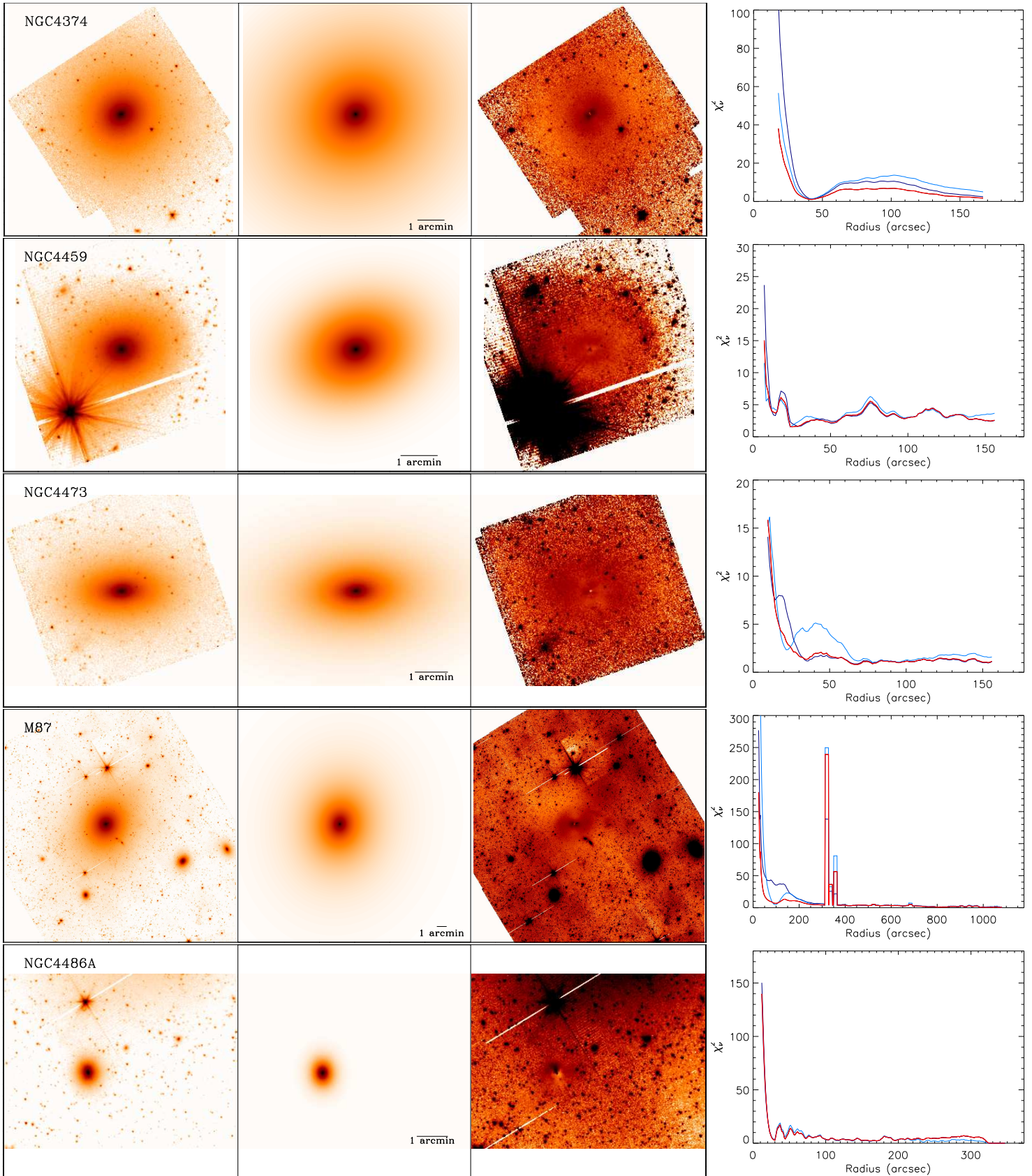


Figure A1. Continued.

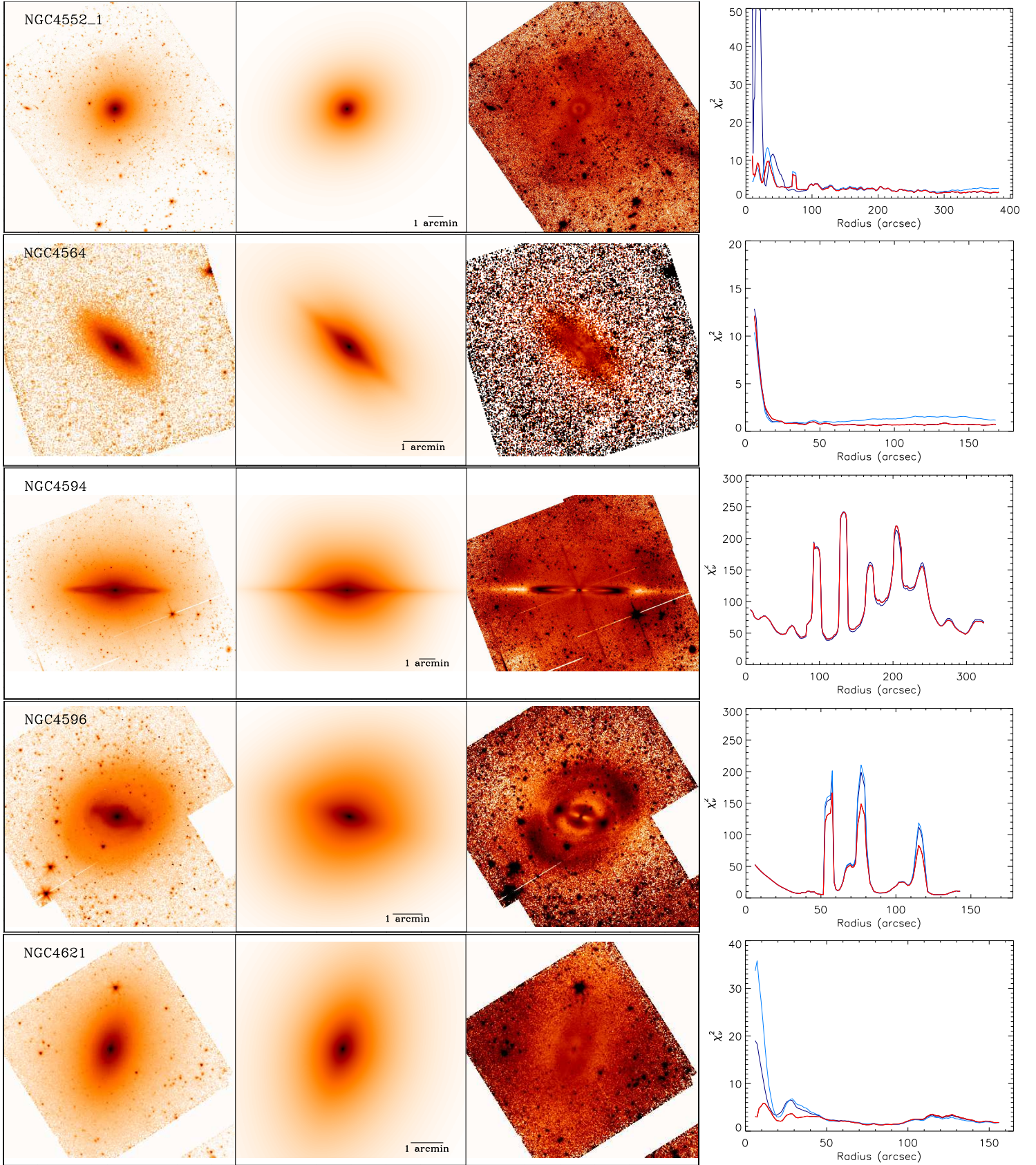


Figure A2. Continued.

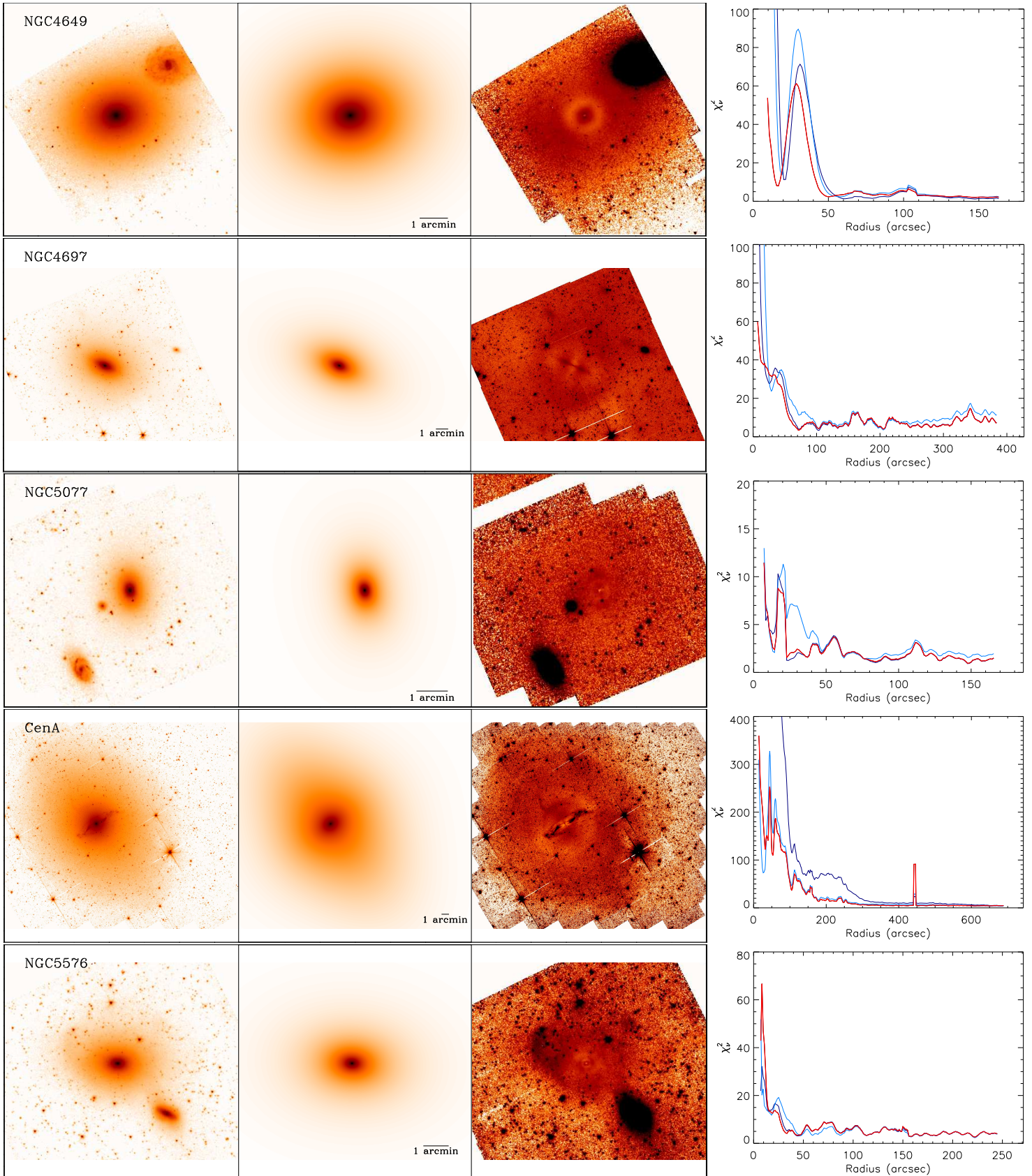


Figure A3. Continued.

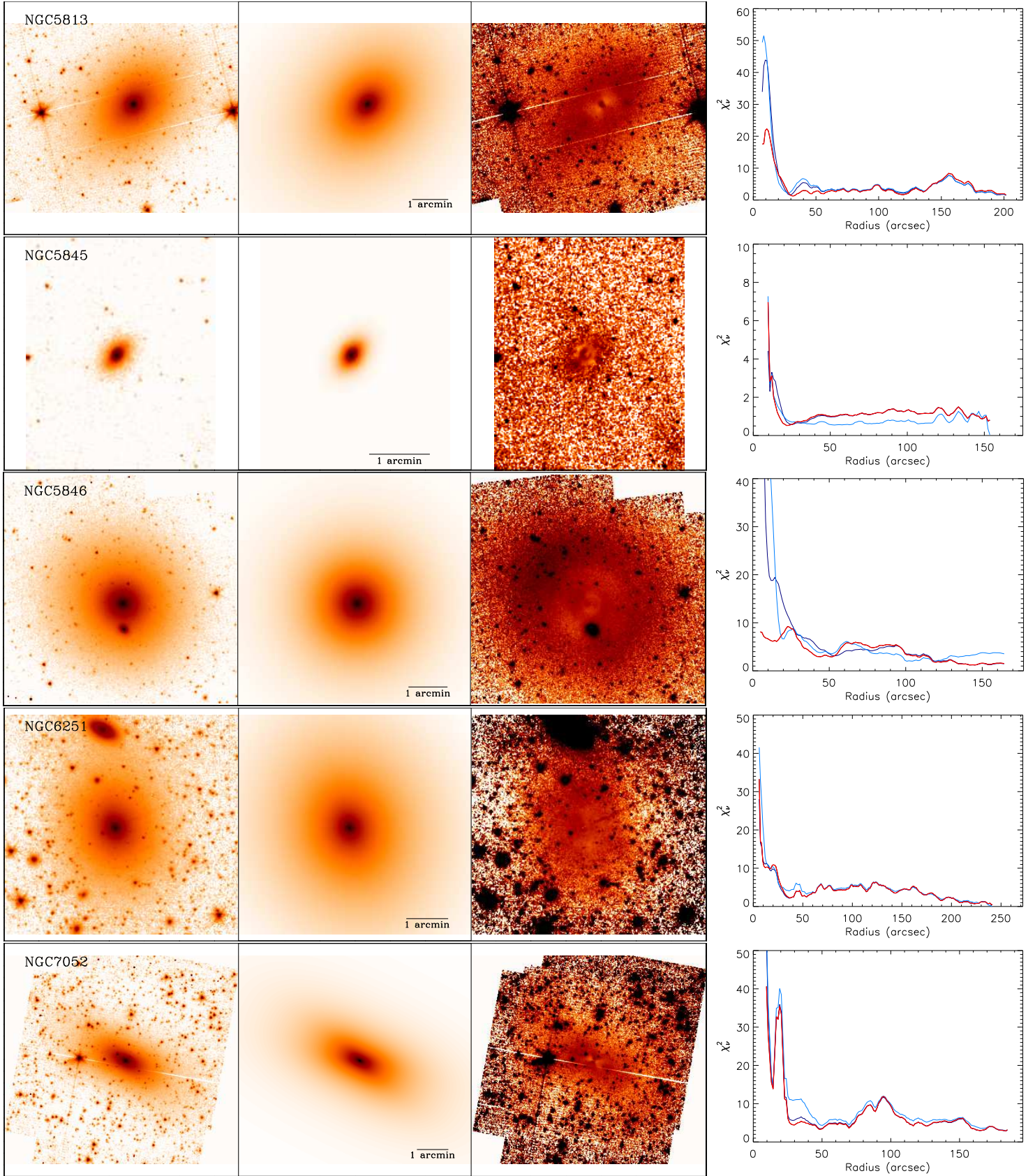


Figure A4. Continued.

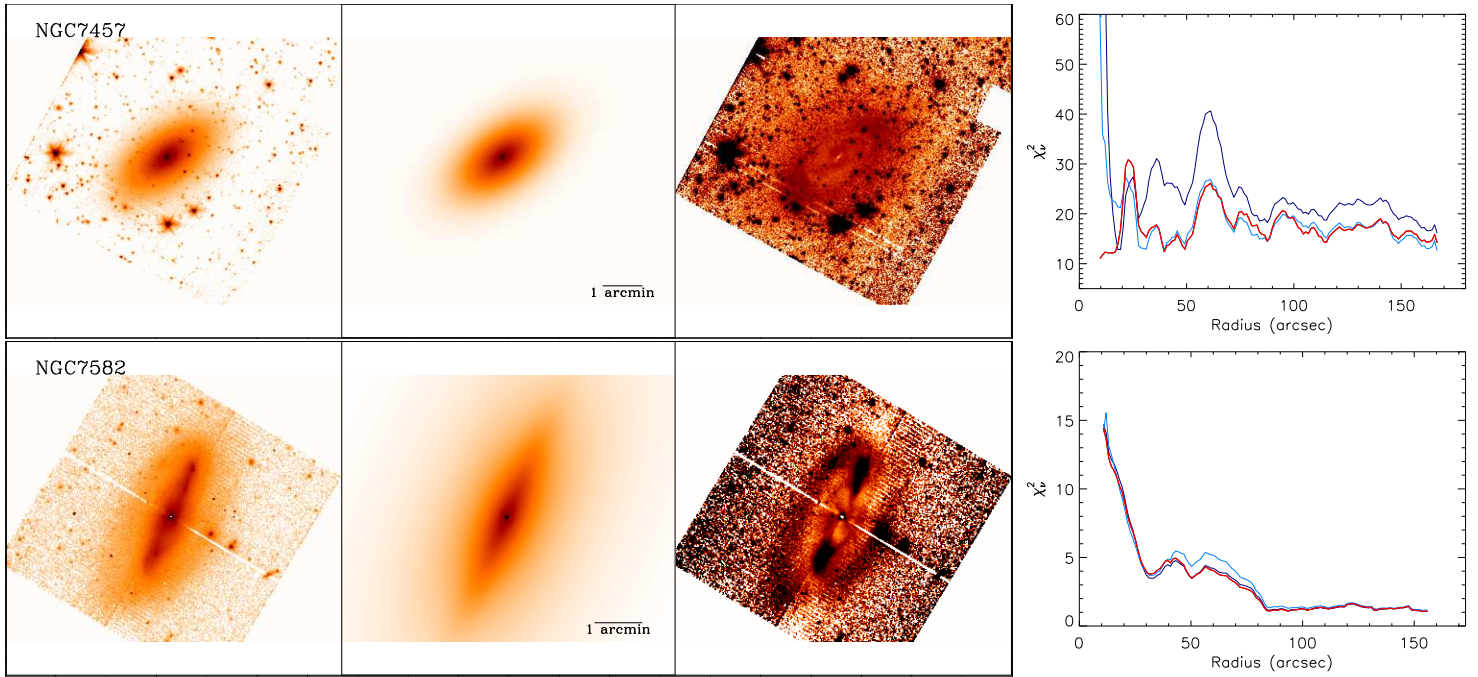


Figure A5. Continued.